

# Advances in Micro-Mechanical Modeling Using a Bonded-Particle Model and Periodic Homogenization Within Discrete Element Framework Applied to Heterogeneous Ceramics

Farid ASADI<sup>a,b\*</sup>, Damien ANDRÉ<sup>a</sup>, Sacha EMAM<sup>c</sup>, Pascal DOUMALIN<sup>d</sup>, Marc HUGER<sup>a</sup>

<sup>a</sup> IRCER Laboratory, UMR CNRS 7315, Université de Limoges, Limoges, France

<sup>b</sup> ArcelorMittal Global Research and Development, Maizières-lès-Metz, France

<sup>c</sup> ITASCA Consultants S.A.S., Lyon, France

<sup>d</sup> PPRIME Institute, UPR CNRS 3346, Université de Poitiers, Chasseneuil, France

## Abstract

The Discrete Element Method (DEM) can account for microcracks initiations and propagations within the microstructure and their impact on the macroscopic properties of ceramics. Combing the DEM with the Periodic Homogenization (PH) allows working with a limited number of elements, thus facilitating the multiscale transition of the elastic properties of ceramics: from the microscale (inclusion/pores scale) to the macroscopic elastic behavior of such continuum media. However, the PH approach for a continuum media is currently less developed in DEM than the FEM. Hence, this study aims to consolidate a DEM framework, using a bonded-particle model and PH to improve the prediction of the elastic properties ( $C_{ij}$  tensor) of ceramics.

Here, a face-centered cubic unit cell is combining with periodic boundary conditions to build a 3D representative volume element in DEM to model the macroscopic elastic properties of model materials and is validated by experimental data, analytical and FEM approaches.

*Keywords:* Discrete element method (DEM), Refractory ceramics, Periodic homogenization, Two-phase materials, Anisotropy

# 1 Introduction

The prediction of elastic behavior of heterogeneous and multiphase materials, such as concretes, rocks, and ceramics, is complicated due to their complex microstructures, which will influence the apparent behavior of these types of composite materials. A preliminary step for predicting such materials' behavior is understanding their microstructures, their constitutive elements, and their interactions. By knowing the properties of the constitutive elements, it is possible to use analytical formulas, such as Hashin and Shtrikman (HS) method [1] [2], or numerical methods, such as Finite Element Method (FEM) simulations, to predict the apparent behavior of the multiphase and porous materials [3] [4].

However, in the case of heterogeneous brittle materials, which could be damaged, due to external mechanical loads or to internal stresses caused by thermal loading, an extensive microcrack network may appear and could have a significant impact on the apparent elastic properties. In such a quite common case, the HS formulas will thus have a noticeable disagreement with the experimental data [5] [6]. On the other hand, due to a very high number of discontinuities, it could be challenging to anticipate the correct value for the elastic parameters of the material by using FEM simulations because such a method has some difficulties dealing with discontinuities [7].

In this context, the Discrete Element Method (DEM) is an adequate alternative numerical method as it can simultaneously manage many cracks initiation and propagation (contacts debonding). At the very beginning, the DEM method was, in fact, introduced to reproduce the mechanical behavior of intact rocks accounting for their complex microstructure in 1971 [8]. Later on, DEM has been developed further and became more practical for simulating the fracturing mechanism and crack propagation, especially for brittle materials [9] [10] [11] [12]. In this way, different bonded particle models [13] were introduced, such as the Flat-Joint model [14], which is today a popular model within the DEM community to simulate brittle and pseudo-brittle materials [15] [16].

The present study proposes to develop and apply a homogenization approach within DEM. The homogenization technique is a powerful way to calculate macroscopic properties with only a small representative volume element but using a specific boundary condition. The main interest of this approach is to predict and scale up the elastic properties of multiphase materials taking into account their heterogeneous microstructure. In the class of the discrete numerical approaches, the homogenization technique was first proposed for molecular dynamics problems in 1981 [17], which is based on the same framework comparing to the DEM approach. Nevertheless, the homogenization technique applied to DEM is much less documented in the literature today than FEM. Especially, there are very few studies dedicated to DEM simulation of heterogeneous continuum media by using the homogenization technique.

For this paper, a homogenization approach was implemented and validated by using the periodic homogenization technique. In the proposed technique, a representative volume element of a two-phase material was designed based on a face-centered cubic arrangement of inclusions within a matrix, combined with periodic boundary conditions (PBC). Moreover, as the local input parameters are different from materials apparent properties in DEM, the different constitutive elements were calibrated separately to reproduce the desired apparent properties.

To validate the proposed approach, results were compared to apparent properties experimentally measured on model materials with simplified microstructure: two-phase and porous materials [5]. The produced samples of these two model materials had different inclusion fractions or porosities, which were compared to the proposed DEM numerical

approach. The result of this comparison is being discussed. Also, to compare the accuracy and the efficiency of the proposed DEM models, the obtained results for elastic properties were compared to analytical HS bounds and FEM simulations, too. In the end, the stiffness tensors of each analytical and numerical method were calculated and compared to the DEM model.

## **2 The motivation of using periodic homogenization within the Discrete Element Method (DEM) to describe the behavior of heterogeneous microstructures**

In this section, the motivation of using periodic homogenization in DEM to describe the macroscopic behavior of heterogeneous materials will be explained. At first, the context of materials with heterogeneous microstructure containing microcracks, such as refractory ceramics, will be introduced. Then, the limitations of FEM to simulate numerous microcracks will be discussed. The chosen DEM contact model to simulate microstructure (Flat-Joint Model) will be introduced, and the current state of homogenization technique in DEM will be briefly discussed. Finally, the reference two-phase model material will be introduced.

### **2.1 Context of materials with heterogeneous microstructure containing micro-cracks**

In the context of ceramic materials currently used as refractory linings of industrial vessels required for the production of steel, glass, as well as cement, a high number of research works has pointed out that the microstructure design of refractories has a significant influence on their ability to sustain thermal shocks in the application. However, understanding this phenomenon is not an easy task due to the complex microstructures of these heterogeneous ceramic materials. Industrial and academic studies have then been launched to understand better how thermal shock resistance can be improved. Such improved resistance was first correlated to an increased toughness. Then, it became clear that the thermal expansion mismatch between constituents (large aggregates within a matrix), entailing microcracking around the aggregates, was mainly responsible for improved thermal shock resistance [18]. Therefore, to define the most suitable microstructure design, a rational experimental procedure of optimization has been considered working with simplified materials containing only a limited number of constituents. The target was to understand better the strong relationships between such complex microstructures and the macroscopic thermomechanical behavior of the materials. Despite their simplified microstructure, these model materials should exhibit a thermomechanical behavior that can mimic some aspects of the behavior of industrial refractories [5].

Beyond this experimental procedure of optimization, it is clear that numerical modeling, like DEM (which could simulate numerous microcracking simultaneously), can also help to build a better understanding of such complex phenomena. In a first step, the present work aims to demonstrate that such a DEM approach, based on a quasi-isotropic Representative Volume Element (RVE) combined with periodic homogenization, is well adapted to simulate the elastic behavior of two-phase and porous materials (without damage). In a second step (not presented here), thermal damage resulting from thermal expansion mismatch between constituents will

be later introduced to study the effect on thermal shock resistance. The possible damage progression, which makes simulations much more complicated, could be thus quite easily introduced in the DEM model to handle the real case of heterogeneous materials.

## **2.2 Limitation of FEM to represent microstructure containing microcracks**

As a widespread mathematical technique for solving partial differential equations, the Finite Element Method (FEM) is a well-known multidisciplinary numerical method for simulating and predicting the physical behaviors of continuum media. In particular, FEM is mostly applied to study the mechanical and thermomechanical behavior of materials. However, for studying the microstructure of materials, which contains numerous discontinuities, FEM could be inadequate. To solve this problem and to introduce arbitrary crack propagation, the Extended Finite Element Method (XFEM) was introduced by Belytschko et al. and Moës et al. in 1999 [19] [20] [21]. Many studies about microcracks and crack propagations using XFEM can be cited. Souza et al., have developed a multiscale model for the transition of local cracks to the macrocracks by using XFEM to model cohesive zones [22]. As another example, Goyal et al. used XFEM to model crack propagations in an aluminum alloy in a uniaxial tensile test [23]. However, XFEM is not able to manage multiple crack initiation and propagation at the same time.

Considering the difficulties of managing multiple crack propagation with the FEM approach, an alternative way is to use the DEM approach, which is more familiar for granular media but can present some critical advantages for modeling the fracturing process in continuous media.

Based on a study by Sharafisafa et al., for simulation of crack propagation in the brittle materials, DEM could simulate realistic secondary crack branching (propagating from the main crack path). In contrast, the secondary cracks were not observed in XFEM models. Furthermore, DEM could simulate the entire process of crack initiation, propagation, and, more importantly, the coalescence of the fracture, but there were many difficulties to reproduce coalescence by XFEM reliably [24]. In another study by Hedjazi et al., for simulating crack branching in a dense vitreous material, it was shown that DEM results were closer to the analytical models in comparison to FEM, and it was more in accordance with experimental visual observation for crack branching in certain conditions [25].

Simulating quantitatively a continuum media with DEM is not as easy as with FEM because the continuum mechanics cannot be introduced directly into the DEM models. On the other hand, as mentioned, simulating discontinuities such as fractures or damages are more straightforward to reproduce in DEM frameworks because of the discrete nature of discontinuous phenomena [26] [27]. Therefore, this study focuses on the continuum modeling with DEM, which is the most challenging part. Hence, at this stage, this paper will not consider fracture initiation and propagation.

## **2.3 DEM to model microstructure properties relationship using Flat-Joint Model (FJM)**

DEM numerical method was initially designed to reproduce intact rocks regarding their microstructure by Cundall in 1971 [8][28]. The code used in this study is the Particle Flow Code (PFC). PFC uses Newton's second law and force-displacement laws at the contacts to

calculate force and the motions of the particles [29]. At first, PFC was designed for granular assemblies without bonding [30]; however, in 2004, the bonded particle model (BPM) was introduced to its contact models [13]. By bonding particles, it was possible to simulate pseudo-continuum media, such as intact rocks [31]. Based on the studies of Cho et al. in 2007, two main bond models of PFC, linear contact bond and parallel bond models were investigated. It was shown that these models had some limitations, namely: the tensile strength to compressive strength ratio was not following the laboratory tests [32].

In 2012, Flat-Joint Model (FJM) was introduced as one of the BPMs models in PFC [33], which improved the mentioned limitations. Different studies were done by using FJM to show its advantage over the other BPM models, for example, matching the compressive to tensile strength ratio to the real granite sample [34] and the perforation failure in the sandstone by Potyondy [14]. Considering these improvements, the FJM was chosen as the contact model for the present study.

In the FJM model, the behavior of the bonded model is linear elastic until a strength limit is reached [29]. As the present study is only investigating the elastic behavior of undamaged two-phase material, the fracture or debonding parameters were not included in the calibration process. There are eight modifiable parameters in FJM; nevertheless, as we are simulating undamaged materials, only three independent parameters were used here to calibrate the apparent behavior of the material:

Initial gap: this parameter defines the maximum distance between two discrete elements for having a bonded FJM contact configuration.

Local Young's modulus of bond: this elastic parameter is defined as the effective elastic modulus at the contact.

Local stiffness ratio of bond: this elastic parameter is defined as the ratio between the normal and the shear local stiffnesses.

For this study, the normal stiffness and shear stiffness of the contacts were set based on the assigned deformability (using local Young's modulus and stiffness ratio). Table 1 shows the list of FJM parameters that were used in this study.

To be more explicit, the local input parameters of the contact model will be marked by 'loc' in superscript. If the parameters refer to the apparent elastic properties of the specimen, it will be shown by 'ap' in superscript. It is important to note that these different parameters should be calibrated in order to fit material elastic properties such as Young's modulus or Poisson's ratio.

Table 1. The input parameters in the Flat Joint contact model.

Parameter description	Symbol	Unit
Initial gap	$g_i^{loc}$	m
Normal stiffness of bond	$K_n^{loc}$	N/m
Shear stiffness of bond	$K_s^{loc}$	N/m
Local Young's modulus of bond	$E^{*loc}$	GPa
Local stiffness ratio ( $K_n^{loc}/K_s^{loc}$ ) of bond	$K^{*loc}$	-

## 2.4 The current state of homogenization technique applies to DEM

The homogenization technique was developed in 1978 by Papanicolau and Bensoussan [35]. This mathematical technique, coupled with numerical methods, is used for the scale transition

of material properties from a local scale (micro) to a global scale (macro). For instance, in a particle-based simulation, even to upscale the behavior of a clay matrix from the nanoscale, a self-consistent homogenization approach could be used [36]. Homogenization had been used for a long time in the FEM models. However, it is relatively less popular in the DEM approach applied to continuum media. During the 1980s, periodic conditions were introduced for molecular dynamics, which is quite close to DEM, to remove the boundaries limitations by [17] and [37]. Later, it was proposed in DEM simulation to apply strains on specimens without imposing boundary effects [38].

In fact, there is a lack of studies for homogenization techniques within DEM, especially in a 3D space. Therefore, the primary motivation of this paper was to implement a periodic homogenization technique in the DEM model for predicting the apparent elastic properties of a simplified microstructure, such as two-phase and porous materials. This study should be considered as the very first stage to validate such a homogenization technique before introducing crack propagations within the model.

## 2.5 Description of reference (uncracked) two-phase and porous model materials

The microstructures of ceramics materials are having complex couplings (for example, physicochemistry couplings) between aggregates and matrix, which affect different macroscopic properties of the material. Thus, to study the elastic properties of two-phase materials, it was necessary to design and produce a simplified material called “model material”. In such simplified materials, only the thermomechanical interactions of two solid phases are expected. This simplification was required in order to clearly observe the effect of increasing the inclusions fraction (or porosity) on the elastic macroscopic response of the materials.

To study elastic behavior of the two-phase material regarding the inclusions fraction and porosity, Tessier-Doyen et al. [6] have designed and built two two-phase “model materials”:

- *Two-phase material with solid inclusions:* Glass matrix with Alumina inclusions (G/A). This model material is made from the composition of a dense aluminosilicate glass matrix containing randomly distributed single-sized spherical alumina beads (with a mean diameter of 500  $\mu\text{m}$ ). The elastic properties of each phase are shown in Table 2. These two solid-phase materials can reproduce a simple isotropic microstructure. The Coefficient of Thermal Expansions (CTE) of both phases are quite close to each other ( $6.5 \times 10^{-6} K^{-1}$  for glass and  $7.6 \times 10^{-6} K^{-1}$  for alumina beads). This close CTE values prevent microcracking or debonding between matrix and inclusions during the cooling down process after the sintering of this two-phase material [5]. Different samples of this material have been produced by varying inclusion fractions in order to observe the effect on the apparent elastic behavior of the material. The microstructure of this model material has been shown in Fig. 1 (a) for 28% of the inclusion volume fraction.
- *Porous two-phase material:* Glass matrix with Pores (G/P). This material is a dense aluminosilicate glass matrix (the same as for G/A material) containing randomly distributed isolated spherical pores [5]. These pores were introduced by using pore-forming agents without inducing any microcracks. Different samples of this material have been produced by varying the porosity in order to observe the effect on the apparent elastic behavior of the material. Nonetheless, due to experimental limitations, the maximum porosity was about 42%. In fact, higher values were inducing interconnected

pores. The microstructure of this model material has been shown in Fig. 1 (b) for the porosity of 18%.

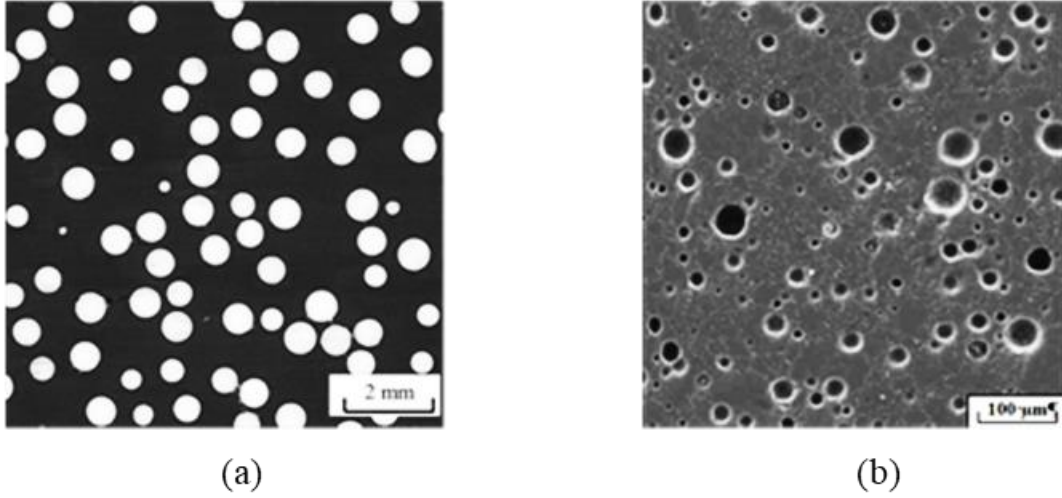


Fig. 1. Model two-phase materials: (a) glass matrix with spherical alumina inclusions, and (b) glass matrix with isolated spherical pores [5].

Table 2. Measured properties of constituents of model two-phase materials [5].

	Property	Measured model material property
Matrix (Glass)	Young's modulus	78 GPa
	Poisson's ratio	0.206
Inclusions (Alumina)	Young's modulus	340 GPa
	Poisson's ratio	0.240

### 3 Numerical methods for homogenization applied to DEM

In this section, the numerical methods and techniques which are required to apply the homogenization to DEM models are explained. At first, the periodic boundary conditions (PBC) were described. Then, a Representative Volume Elements (RVE) was chosen and built to be used in the periodic conditions. In order to obtain apparent properties of RVE, it was necessary to load the sample mechanically. Therefore, the required techniques to load the numerical sample and measuring the apparent properties were explained. Afterward, the calibration process in the PBC was explained. At the end of this section, the computational method to calculate RVE's apparent stiffness tensor was introduced.

#### 3.1 Periodic Boundary Conditions (PBC) in the Discrete Element Method (DEM)

In numerical models, periodic boundaries are often used to remove free boundary effects [38]. Theoretically, in a PBC applied to a DEM model, if a discrete element centroid goes outside the periodic boundary box, it translates back to the opposite face of the box. In order to

ensure contacts between elements located at opposite faces (or corners) of the boundary, “ghost” elements are introduced [29]. The ghost elements are shown in red in Fig. 2 for a perfect 2D square RVE. The blue square at the center of the picture is called a unit cell.

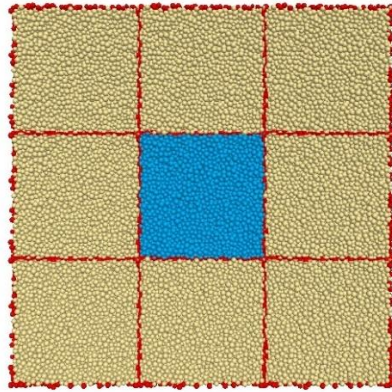


Fig. 2. A square specimen in PBC (in 2D). Ghost elements and PBC borders are shown in red. The main RVE is in blue (only 8 copies are shown here in 2D; However, 26 copies should be considered in 3D).

### 3.2 Creating Representative Volume Elements (RVE)

For building the unit cell in the periodic 3D space for homogenization technique, it was necessary to choose a periodic microstructure arrangement that induces a low degree of anisotropy in order to reproduce a statistically isotropic behavior of the two-phase material (see section 2.5). Based on the previous studies, a Face-Centered Cubic (FCC) arrangement had shown a low degree of anisotropy for periodic homogenization [4]. Therefore, the FCC arrangement has been chosen for the present study to represent a two-phase material (matrix-inclusion system) RVE. In Fig. 3, the matrix is shown in blue, and the inclusions are in grey.

For creating a two-phase RVE with two different constituents, it was necessary to assign different contact (local) properties for the matrix and inclusions regions. As will be mentioned in the calibration part (see section 3.6), local values were obtained independently by going through the calibration process in PBC for each constituent separately. The interface properties (the contacts between inclusion elements and matrix elements) could be assigned as the matrix, the inclusions, or other desired properties. In this study, for these interface contacts, the matrix properties have been assigned. In other words, no particular property was given to the interface. In fact, in the present case for which no particular properties have been targeted for the interface during the processing of the model material, and thus promoting a very well bond of the glass matrix (by sintering) on the surface of the Alumina beads, properties of the interface could assume similar to the matrix. This point is also in line with the reference analytical model, the Hashin-Shtrikman (see section 4.1.2), which doesn't consider any particular properties at the interface and only considers the intrinsic properties of the two phases with their volume fraction. The contact network is shown in Fig. 3 (c), where the interface contacts are specifically shown in red.

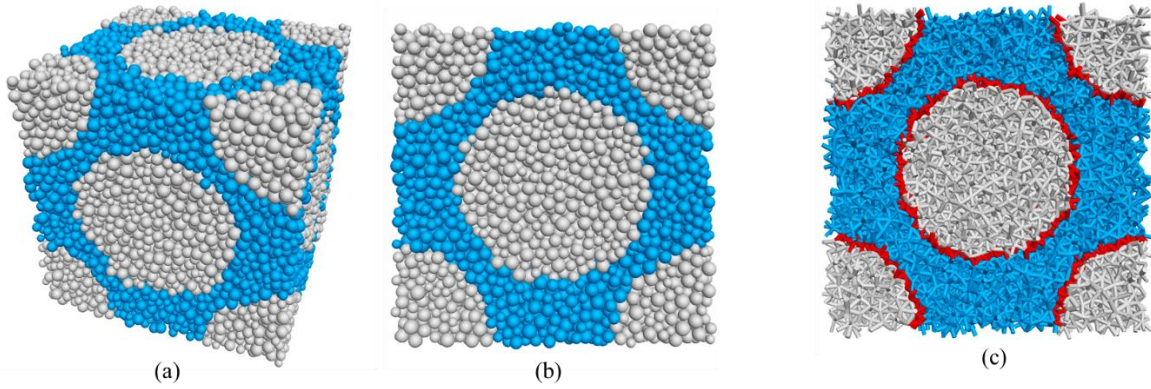


Fig. 3. FCC arrangement: (a) and (b) numerical sample produced by around 20k discrete elements, and (c) the contacts among the discrete elements.

It is noteworthy to mention that the total number of 20k discrete elements was enough for this RVE, considering the computation time efficiency and accuracy of results. Further detail about the procedure to choose the number of elements is discussed in section 4.2.2.

The proposed study aims to compare the influence of the inclusion volume fraction on the apparent elastic properties of the model with an analytical model and experimental observations. In such a perspective, several inclusion radii were considered inside the RVEs (Fig. 4).

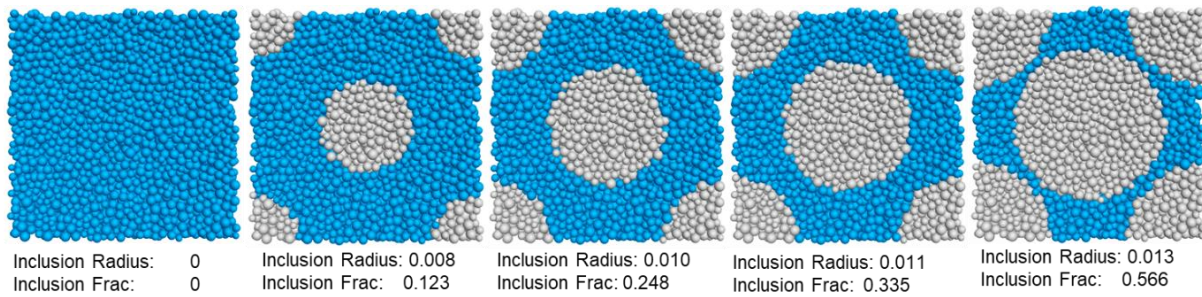


Fig. 4. Inclusion fraction increase from 0% to 57% by FCC arrangement

In the same way, to study the porosity effect, another set of RVEs was built using the same FCC arrangement and replacing the inclusions with voids (Fig. 5 (b)).

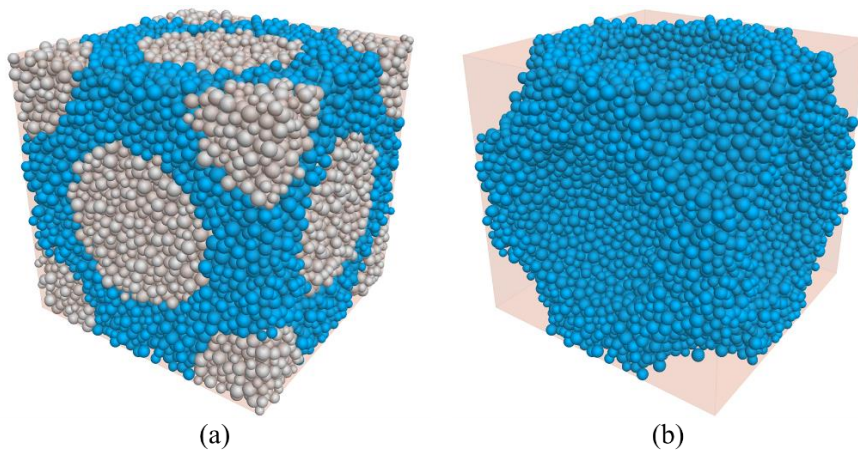


Fig. 5. Side-by-side comparison of simulated FCC-arranged RVEs in periodic space: (a) two-phase material (b) porous material

### 3.3 Distortion technique of PBC for applying strain to RVE

In order to measure numerically apparent properties of RVE, it was necessary to load the sample mechanically. In the case of periodic boundaries, this loading should be applied with particular conditions named “domain distortion technique” in PFC. Initially, the concept of distortion of boundary conditions was introduced by Parrinello and Rahman for molecular dynamics in 1981 [17]. Later, this technique was adapted to DEM simulation to apply strains on specimens without imposing boundary effects [38].

In this paper, this method was used to load the RVEs by distorting the PBC in the loading direction while keeping the PBC shape parallelepipedic. The PBC is also distorted in the other directions to ensure pure loading modes (pure tension and pure/simple shear). In such a case, the deformation of the PBC is modeled by imposing a uniform strain-rate field over the discrete elements, which is coming from the equation of the motions. In addition, damping is introduced to minimize the dynamic effects (such as oscillations). This point has been explained more in detail in section 3.5. A detailed description of the distortion of PBC in PFC is described in the literature [39] [40].

### 3.4 Measurement sphere technique to obtain global stress within RVE

In this study, the discrete domain is considered as a pseudo-continuum media. However, the medium is still discrete, so it is impossible to calculate stress directly, as stress is a continuum quantity. Hence, in order to measure apparent properties during a test, such as stresses or strains, the “measurement sphere” technic was applied.

The measurement sphere consists of a virtual sphere that measures a given quantity such as stress or strain in a specified DEM model region. It gives the average values of the assigned measurable quantities, such as stress tensor, strain rate, and porosity [29]. In this study, only the stress tensors were measured by using this technique, while the strain was computed from the imposed PBC strain-rate.

To obtain the stress, an averaging procedure is used to convert local forces to a continuum apparent stress of the RVE. The average stress  $\bar{\sigma}_{ij}$  in a measurement region of volume  $V$  is computed as [41]:

$$[\bar{\sigma}] = -\frac{1}{V} \sum_{N_c} \mathbf{F}^{(c)} \otimes \mathbf{L}^{(c)} \quad \text{Eq. 1}$$

where  $N_c$  is the number of contacts in the specified region,  $\mathbf{F}^{(c)}$  is the contact force vector,  $\mathbf{L}^{(c)}$  is the branch vector between the centroids of the two bodies in contact and  $\otimes$  is the outer product.

### 3.5 Servo-Control technique for applying uniaxial tensile test

In this study, virtual uniaxial tensile tests were used for the macroscopic elastic parameter’s calibration. These uniaxial tensile tests should be performed by distorting the PBC with a constant small strain-rate in the direction of the loading. In PBC, this strain-controlled condition is applied by distorting the PBC in one direction while using the servo-control mechanism to distort the two other directions. In the perpendicular directions to the strain-controlled one, this

servo-control technique ensures maintaining a small constant value of user-defined confining stresses during the test by distorting the PBC.

These confining stresses within the sample are monitored continuously by using the measurement sphere. Then, the strain-rate is adjusted in order to keep constant these confined stresses at low user-defined values. For each direction, this strain rate can be computed as:

$$\dot{\varepsilon} = G (\sigma^t + \sigma^r) \quad \text{Eq. 2}$$

where,  $\dot{\varepsilon}$ ,  $G$ ,  $\sigma^t$  and  $\sigma^r$  are strain rate, controller gain, the user-defined confining stresses, and reaction stress (coming from the response of the sample), respectively. The controller gain ( $G$ ) is a proportional controller. The mechanism of the servo-control technique is explained more in detail in [29].

### 3.6 Calibration of local properties for each constituent

FJM was successfully used for simulations of brittle and quasi-brittle materials. However, there is no well-defined relationship between the contact properties (the local parameters of the bonds between discrete elements) and the elastic properties of the material. Hence, the FJM requires a calibration process to assign the correct values for the contact properties to reproduce the desired apparent elastic properties [42][43]. As mentioned in section 2.3, the main input parameters for the FJM are the local Young's modulus ( $E^{*loc}$ ) and the local stiffness ratio ( $K^{*loc}$ ); which must match the elastic properties of the material to the model. For an elastic isotropic material, the apparent Young's modulus ( $E^{ap}$ ) and the apparent Poisson's ratio ( $\nu^{ap}$ ) must be targeted. In addition to the mentioned parameters, the input values for the calibration also depend on the initial gap, the number of the discrete elements (size and/or discretization fineness of the model) and in some case, the sample shape. Therefore, these parameters should be set and fix initially before beginning the calibration process. So, as this model aimed to be used in the PBC, the calibration process must be done with PBC.

The calibration process was done on a cubic sample, consists of around 20k discrete elements. The process of choosing this number of elements has been explained in section 4.2.2. The calibration of FJM contact model parameters follows a systematic approach as explained here step by step:

1. *Initial gap ( $g_i^{loc}$ )*: Assigning a small value for the bonding gap will result in not having the same elastic properties in the uniaxial tensile test (tensile behavior) and in the uniaxial compression test (compressive behavior) which is not realistic. To simplify the calibration process, the value for the initial gap was defined as a fraction of the average discrete element diameter (ball). This fraction had to be high enough to reproduce the same elastic properties both in tension and compression. By testing different values for this fraction, the minimum value which satisfies mentioned condition was 0.4 of the average discrete element's diameters.
2. *Local stiffness ratio ( $K^{*loc}$ )*: The local stiffness ratio ( $K^{*loc}$ ) should be calibrated before the local Young's modulus ( $E^{*loc}$ ), as effective local Young's modulus, does not affect the apparent Poisson's ratio ( $\nu^{ap}$ ) [43]. Hence, in a trial and error process and by measuring the apparent Poisson's ratio ( $\nu^{ap}$ ) in the uniaxial tensile test, the local stiffness ratio ( $K^{*loc}$ ) set to a value which could produce the targeted apparent Poisson's ratio ( $\nu^{ap}$ ).

3. *Local Young's modulus ( $E^{*loc}$ )*: After calibrating and fixing the local stiffness ratio ( $K^{*loc}$ ), in a trial and error process and by measuring the apparent Young's modulus ( $E^{ap}$ ) in the uniaxial tensile test, the local Young's modulus ( $E^{*loc}$ ) set to a value which could produce the targeted apparent Young's modulus ( $E^{ap}$ ).

The modified proposed FJM calibration algorithm for this study was based on the algorithm proposed in [42] and [43]. It is summarized in Fig. 6.

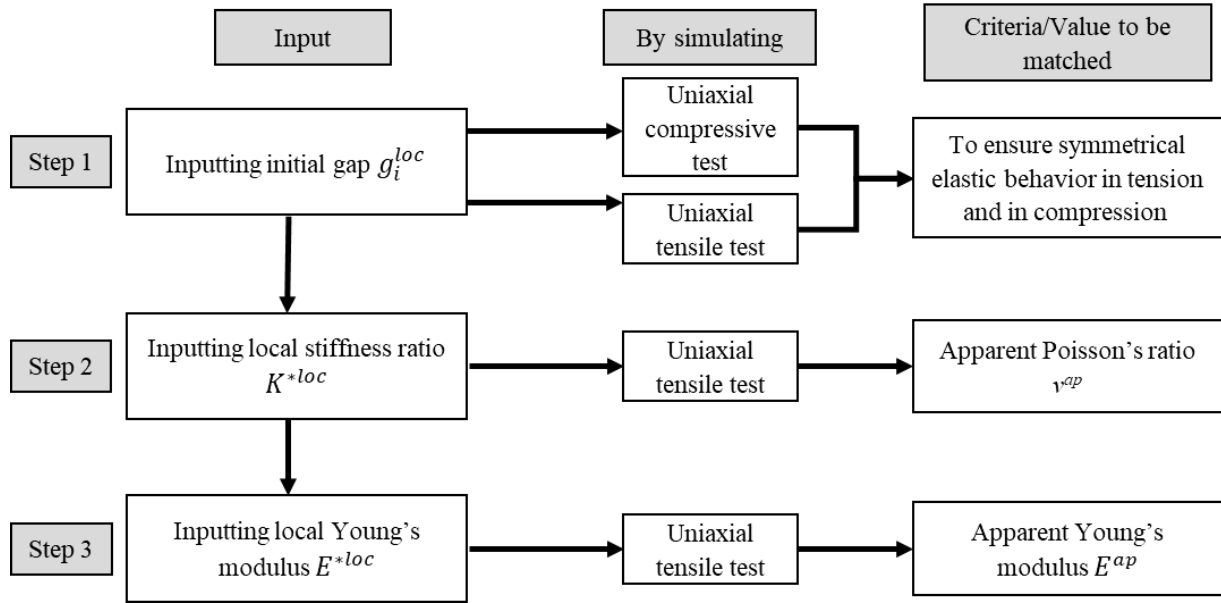


Fig. 6. The modified algorithm to calibrate elastic parameters of the RVE in PBC inspired by Vellojes et al. [42].

To build up the two-phase materials, firstly, it was necessary to go through the calibration process for each constituent separately (Glass matrix and Alumina inclusions) to reproduce their own apparent elastic properties. In Table 3, the input parameters and the apparent parameters for each pure constituent are summarized.

Table 3. The input parameters and apparent properties of the two-phase material

Targeted Experimental Material property		FJM input parameter		Simulated Apparent Material property		
Description	Value	Description	Value	Description	Value	
Reproduce symmetrical elastic behavior in tension and compression		-	Initial gap ( $g_i^{loc}$ )	40% of the avg. balls radius	Reproduce symmetrical elastic behavior in tension and compression	Achieved
Matrix (Glass)	Young's modulus	78 GPa	local Young's modulus ( $E^{*loc}$ )	88.2	Apparent Young's modulus ( $E^{ap}$ )	78 GPa
	Poisson's ratio	0.206	local stiffness ratio ( $K^{*loc}$ )	5.6	Apparent Poisson's ratio ( $\nu^{ap}$ )	0.2060
Inclusions (Alumina)	Young's modulus	340 GPa	local Young's modulus ( $E^{*loc}$ )	438.8	Apparent Young's modulus ( $E^{ap}$ )	340 GPa
	Poisson's ratio	0.24	local stiffness ratio ( $K^{*loc}$ )	12.1	Apparent Poisson's ratio ( $\nu^{ap}$ )	0.2400

It should be mentioned that with free boundary conditions (without considering the periodic homogenization), the geometry of the specimen influences the calibration process [44]. After investigation of some other geometries rather than a cube (parallelepiped two times larger in one direction), it should be noted that using periodic homogenization strongly limits the influence of the shape of the sample in the calibration process.

### 3.7 Computational method of RVE's apparent stiffness tensor

For using the periodic homogenization technique, it was necessary to build an RVE with a low degree of anisotropy to match the behavior of the model materials. Therefore, the FCC arrangement was chosen for building the RVEs. On the other hand, the DEM is a model with a random spatial positioning of discrete elements which could not respect a perfect symmetry. In such a case, the random spatial positioning of discrete elements could lead to a certain level of mechanical anisotropy coming from this spatial asymmetry.

To investigate this influence, the effective stiffness tensor of RVEs was calculated by two different approaches for the DEM model RVE: assuming a perfect geometrical planar symmetry in 3D of the sample or not. For the first case, the effective stiffness tensor of the FCC arrangement could be calculated as a cubic symmetry stiffness tensor [45]. For the second case, to investigate the impact of asymmetry, it was essential to measure the apparent elastic properties of RVEs in each main direction of RVE, which are shown in Fig. 7. Hence, the cubic symmetry assumption of the previous approach was not retained, and the orthotropic symmetry assumption was considered. The technical steps to calculate each of these approaches for the DEM models are explained in the following sections.

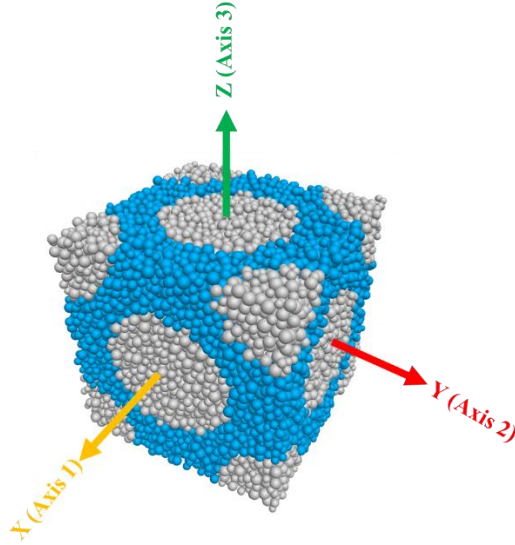


Fig. 7. The main directions of the modeled FCC arranged RVE.

### 3.7.1 Cubic symmetry assumption

By assuming a perfect geometrical planar symmetry in 3D, it was possible to calculate the effective stiffness tensor with three independent elastic elements, as shown in Eq. 3.

$$C_{ij} = \begin{pmatrix} C_{11} & C_{12} & C_{12} & 0 & 0 & 0 \\ & C_{11} & C_{12} & 0 & 0 & 0 \\ & & C_{11} & 0 & 0 & 0 \\ Sym & & & C_{44} & 0 & 0 \\ & & & & 0 & C_{44} \\ & & & & & 0 \\ & & & & & 0 & C_{44} \end{pmatrix} \quad \text{Eq. 3}$$

$$C_{ij} = \begin{pmatrix} E^{ap}(1-\nu)/(1-\nu-2\nu^2) & E^{ap}\nu/(1-\nu-2\nu^2) & E^{ap}\nu/(1-\nu-2\nu^2) & 0 & 0 & 0 \\ & E^{ap}(1-\nu)/(1-\nu-2\nu^2) & E^{ap}\nu/(1-\nu-2\nu^2) & 0 & 0 & 0 \\ & & E^{ap}(1-\nu)/(1-\nu-2\nu^2) & 0 & 0 & 0 \\ Sym & & & E^{ap}(1-\nu)/(1-\nu-2\nu^2) & 0 & 0 \\ & & & & G^{ap} & 0 \\ & & & & & 0 \\ & & & & & 0 & G^{ap} \\ & & & & & & 0 & 0 & G^{ap} \end{pmatrix}$$

For calculating the first two elastic elements in the cubic symmetric stiffness tensor ( $C_{11}$  and  $C_{12}$ ), it was required to measure the apparent properties,  $E^{ap}$  and  $\nu^{ap}$ . To measure apparent Young's modulus ( $E^{ap}$ ) a direct uniaxial tensile test was performed by distorting the PBC with a constant small strain-rate (Fig. 8 (a)). By using a distortion of PBC technique (section 3.3) and measurement sphere (section 3.4), the principal stress within the RVE was measured. Then by having the total applied strain, the apparent Young's modulus ( $E^{ap}$ ) was calculated. The apparent Poisson's ratio ( $\nu^{ap}$ ) could be obtained by measuring the perpendicular strains and by having the applied strain in the T direction, as shown in Fig. 8 (a), which are coming from the distortion of the PBC.

For calculating the last elastic element in the cubic symmetric stiffness tensor ( $C_{44}$ ), the apparent shear modulus ( $G^{ap}$ ) had to be measured. To do so, a simple shear test was performed by distorting the PBC with a constant small shear strain-rate, only in the S (XY) direction, as shown in Fig. 8 (b). At a given applied shear strain, the shear stress was calculated within the

RVE (with respect to the loading direction) using the measurement sphere technique. By having the shear stress and the applied shear strain, the apparent shear modulus ( $G^{ap}$ ) was calculated.

It should be mentioned that, in this case, to ensure that there is no induced strain rather than the one in the imposed shear direction (XY) in the RVE, the servo-control mechanism in the main directions (X, Y and Z) were deactivated. In this way, there will be no imposed strains on the main directions (aimed at maintaining a certain level in the stress in the servo-control mechanism).

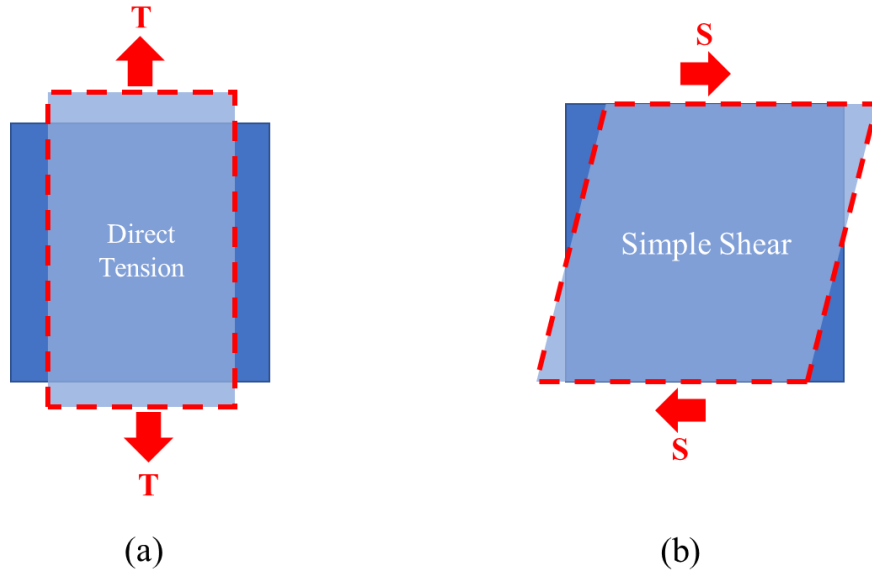


Fig. 8. The schematic of mechanical tests simulation: (a) a uniaxial tensile test simulation in T direction on the numerical sample, and (b) a simple shear test in S direction on the numerical sample.

Finally, after obtaining the apparent Young's modulus ( $E^{ap}$ ), Poisson's ratio ( $\nu^{ap}$ ) and shear modulus ( $G^{ap}$ ), it was possible to use the constitutive law for cubic symmetry as noted in Eq. 3 to calculate  $C_{11}$ ,  $C_{12}$ , and  $C_{44}$  elements and build the stiffness tensor of RVE [46]. The calculation time for each simulation took about 5 to 8 minutes for 20k discrete elements on a system with Intel Core Xeon E2186M 4.0 GHz, SSD, 16 GB RAM, 12 parallel threads.

### 3.7.2 Orthotropic symmetry assumption

This time, it was assumed that there is no perfect geometrical planar symmetry in 3D due to the spatial randomness of the discrete elements positioning. Considering this asymmetry, the cubic symmetry assumption was not considered, and the same RVEs were considered orthotropic, with nine independent elastic coefficients and three mutually perpendicular symmetry planes (as noted in Eq. 4 for the theoretical orthotropic assumption).

$$C_{ij} = \begin{pmatrix} C_{11} & C_{12} & C_{13} & 0 & 0 & 0 \\ & C_{22} & C_{23} & 0 & 0 & 0 \\ & & C_{33} & 0 & 0 & 0 \\ & Sym & & C_{44} & 0 & 0 \\ & & & & 0 & C_{55} \\ & & & & & 0 \\ & & & & & & 0 & 0 & C_{66} \end{pmatrix}$$

$$C_{ij} = \begin{pmatrix} E_{11}^{ap}(1 - \nu_{23}\nu_{32})Y & E_{11}^{ap}(\nu_{21} + \nu_{31}\nu_{23})Y & E_{11}^{ap}(\nu_{31} + \nu_{21}\nu_{32})Y & 0 & 0 & 0 \\ & E_{22}^{ap}(1 - \nu_{13}\nu_{31})Y & E_{22}^{ap}(\nu_{32} + \nu_{12}\nu_{31})Y & 0 & 0 & 0 \\ & & E_{33}^{ap}(1 - \nu_{12}\nu_{21})Y & 0 & 0 & 0 \\ & Sym & & G_{23}^{ap} & 0 & 0 \\ & & & & 0 & G_{13}^{ap} \\ & & & & & & 0 & 0 & G_{12}^{ap} \end{pmatrix} \quad \text{Eq. 4}$$

$$Y = \frac{1}{1 - \nu_{12}\nu_{21} - \nu_{23}\nu_{32} - \nu_{31}\nu_{13} - 2\nu_{21}\nu_{32}\nu_{13}}$$

For calculating the first three elastic elements of the main diagonal ( $C_{11}$ ,  $C_{22}$ , and  $C_{33}$ ), and three off-diagonal symmetric elements ( $C_{12}$ ,  $C_{13}$ , and  $C_{23}$ ), it is required to perform three uniaxial tensile tests on each main axes (Fig. 7). Each of these uniaxial tensile tests gave one of the mentioned main diagonals and one of the off-diagonal elements independently. These uniaxial tensile tests were performed, as explained earlier in the previous section. However, as mentioned in Eq. 4 for orthotropic assumption, in the case of the geometrical cubic sample, the Poisson's ratio ( $\nu^{ap}$ ) should be measured in two perpendicular directions, independently. To satisfy this point, in each simulation for obtaining the elements of the orthotropic matrix, the Poisson's ratio ( $\nu^{ap}$ ) was measured in the two perpendicular directions.

Finally, for calculating the last three independent elements of the main diagonal of orthotropic stiffness tensor ( $C_{44}$ ,  $C_{55}$ , and  $C_{66}$ ), the apparent shear modulus ( $G^{ap}$ ) had to be measured along the three main axes. The procedure of measuring the apparent shear modulus ( $G^{ap}$ ) was explained earlier in the previous section.

After obtaining the apparent Young's modulus ( $E^{ap}$ ), Poisson's ratio ( $\nu^{ap}$ ) and shear modulus ( $G^{ap}$ ), it was possible to use the constitutive law for orthotropic materials as shown in Eq. 4 to calculate the nine elements ( $C_{11}$ ,  $C_{22}$ ,  $C_{33}$ ,  $C_{44}$ ,  $C_{55}$ ,  $C_{66}$ ,  $C_{12}$ ,  $C_{13}$ , and  $C_{23}$ ) and build the stiffness tensor of RVE. [46]

Note that the first three diagonal components ( $C_{11}$ ,  $C_{22}$ ,  $C_{33}$ ) are related to the tension-compression stiffness of the material in the three main directions. The last three diagonal components ( $C_{44}$ ,  $C_{55}$ ,  $C_{66}$ ) are related to the shear stiffness of the material. Also, the three off-diagonal components ( $C_{12}$ ,  $C_{13}$ ,  $C_{23}$ ) are related to the extension-extension coupling. These relations are the same for the cubic assumption as well.

The results of these different approaches were compared in section 4.4 to check the difference between the two assumptions and evaluate the influence of spatial randomness of the discrete elements positioning on the anisotropy degree of the RVEs. Also, in other predictive methods, such as most FEM models, the first approach was used; hence, it was essential to make a comparison between these two approaches, FEM [4] and analytical [2] models, to check the validity of this model.

## 4 Apparent elastic properties result and discussion

Based on the numerical techniques of the previous sections, the applications and results of the DEM simulations in predicting the elastic properties of two-phase and porous materials by using the periodic homogenization approach are presented and discussed in the following parts.

Firstly, the reference values coming from experimental, analytical, and numerical (FEM) results are introduced. Later, a series of numerical investigations are carried out to refine the DEM periodic models. In the end, to validate the accuracy of the DEM models, Young's modulus and Poisson's ratio obtained by DEM using PBC are confronted with reference values.

### 4.1 Reference values coming from experimental works combined with analytical and numerical (FEM) model

To verify the proposed periodic homogenization in the DEM model for two-phase and porous materials, it was essential to confront the obtained results to experimental data and/or other predictive methods such as FEM. Firstly, a comparison is made with experimental results. Secondly, the results are compared to other existing methods, such as an analytical method (by using Hashin and Shtrikman relationships) and a numerical approach (Finite Element Method simulations).

#### 4.1.1 Experimental elastic properties of model two-phase material

As mentioned in section 2.5, two kinds of model materials were studied: a Glass matrix with randomly distributed Alumina inclusions (G/A) and a Glass matrix with randomly distributed spherical Pores (G/P). For the material G/A, different samples were prepared in the study by Tessier-Doyen [6], with different inclusion fractions, as shown in Fig. 9. Similarly, for material G/P, various porosity values were considered.

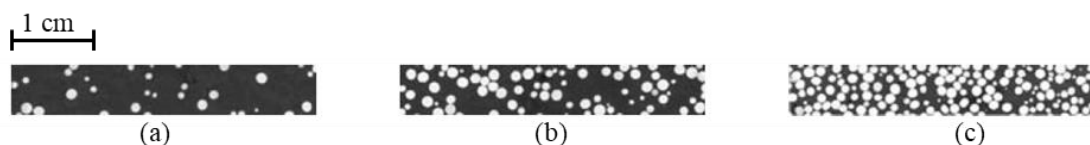


Fig. 9. Optical images of two-phase model material with different inclusion volume fractions: (a) 7 %, (b) 28 % and (c) 48 % [6].

For measuring elastic properties, these model materials were considered isotropic materials at the macroscopic scale. Their elastic properties, Young's modulus, and Poisson's ratio were measured by ultrasonic wave propagation technique with contact transducers. Besides, to limit the attenuation of the waves causing by inclusions or pores, the measurements were done in transmission at low frequency (1 MHz). The same technique was used for G/P materials [5] [6].

#### 4.1.2 Hashin and Shtrikman (HS) bounds for model two-phase and porous materials

To predict analytically elastic properties of the two-phase or porous model materials, Hashin and Shtrikman (HS) model was chosen for this study [2]. This analytical predictive approach defines two bounds for two-phase materials: Hashin and Shtrikman upper bound (HS+) and Hashin and Shtrikman lower bound (HS-).

For the G/A case, as it was mentioned in section 2.5, the inclusions are nearly four times stiffer than the matrix: 78 GPa for matrix and 340 GPa for the inclusions. In such a case, as mentioned in previous studies, Young's modulus and Poisson's ratio should follow the lower HS bound (HS-) while increasing the inclusion volume fraction [47] [6] [48] [49].

For G/P material, which is a porous material, it is assumed that void's bulk modulus ( $K$ ) and shear modulus ( $G$ ) is zero; therefore, the bulk modulus ( $K$ ) and shear modulus ( $G$ ) of the matrix is considered as very high in comparison to the voids. In such a case, the reference given by HS bounds is inverted. This means the HS upper bound (HS+) will be the analytical reference for the porous material, whereas HS lower bound (HS-) is zero [50] [51] [52].

In the HS model, the apparent Young's modulus ( $E^{ap}$ ) and Poisson's ratio ( $\nu^{ap}$ ) can be predicted by knowing the volume fraction of inclusions (or porosity) as well as the bulk and shear modulus of each constituent. The analytical relationships of the Hashin and Shtrikman (HS) model are shown in Table 4. These relationships are used to plot upper and lower Hashin and Shtrikman bounds (HS+ and HS-).

Table 4. The main HS analytical relationships for the elastic properties of a two-phase material

Property	Lower Hashin and Shtrikman bound (HS-)	Upper Hashin and Shtrikman bound (HS+)
Bulk modulus	$K^{HS-} = K_m + \frac{f_i}{\frac{1}{K_i - K_m} + \frac{3(1-f_i)}{3K_m + 4G_m}}$	$K^{HS+} = K_i + \frac{1-f_i}{\frac{1}{K_m - K_i} + \frac{3f_i}{3K_i + 4G_i}}$
Shear modulus	$G^{HS-} = G_m + \frac{f_i}{\frac{1}{G_i - G_m} + \frac{6(K_m + 2G_m)(1-f_i)}{5G_m(3K_m + 4G_m)}}$	$G^{HS+} = G_i + \frac{1-f_i}{\frac{1}{G_m - G_i} + \frac{6(K_i + 2G_i)f_i}{5G_i(3K_i + 4G_i)}}$
Young's modulus	$E^{HS-} = \frac{9K^{HS-} \cdot G^{HS-}}{3K^{HS-} + G^{HS-}}$	$E^{HS+} = \frac{9K^{HS+} \cdot G^{HS+}}{3K^{HS+} + G^{HS+}}$

Table 4 summarizes the analytical formula given by HS where  $f_i$  is the volume fraction of inclusions,  $K_m$  and  $K_i$  are bulk modulus of matrix and inclusions,  $G_m$  and  $G_i$  are shear modulus of matrix and inclusions.

### 4.1.3 Periodic homogenization in the case of Finite Element Method (FEM)

Another reference results come from the study of Grasset-Bourdel et al. [4]. The mentioned two-phase model materials (G/A and G/P) were modeled by finite element periodic homogenization. Here, the FCC arrangement is considered for the RVEs (Fig. 10) [4]. Therefore, both FEM and DEM models simulated the FCC arrangement that made a direct comparison between the FEM and DEM models possible.

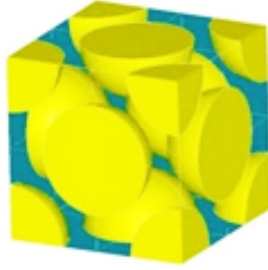


Fig. 10. The continuum RVEs modeled with FEM in Face-Centered Cubic (FCC) arrangement [4]

## 4.2 Numerical investigations for producing DEM periodic homogenization

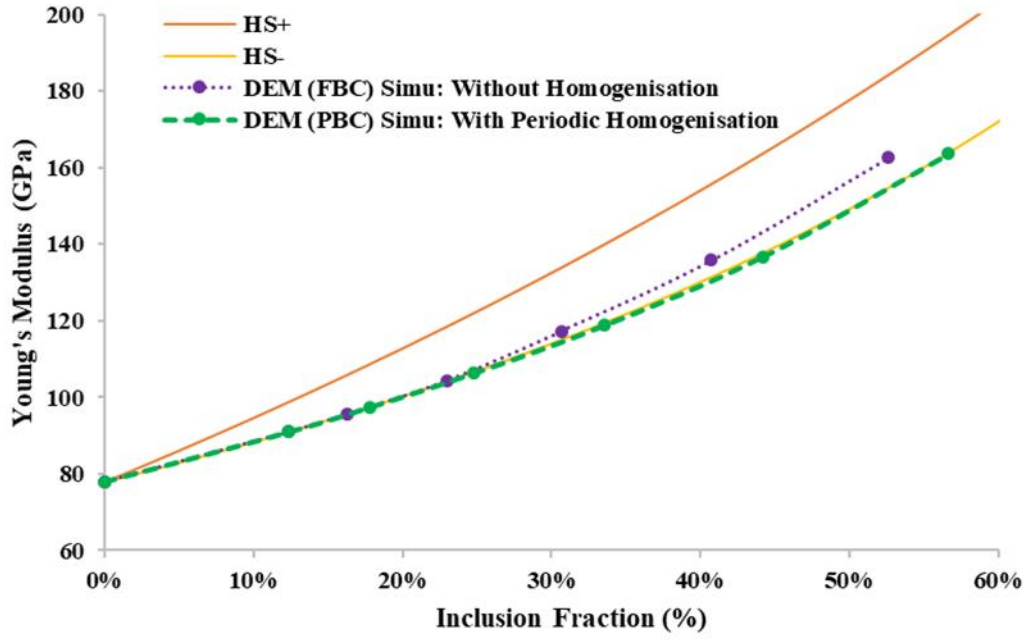
To build an accurate numerical DEM model, the impact of different numerical approaches and techniques has been investigated. In this regard, the influence of using periodic homogenization technique, the impact of the number of discrete elements, and different possible numerical approaches to calculate experimental inclusion volume fraction (and porosity) are investigated. All these points are very well-documented in literature for FEM modeling, but in the specific case of DEM applied to continuous media, these concepts are, in fact, not well established yet.

### 4.2.1 Periodic homogenization

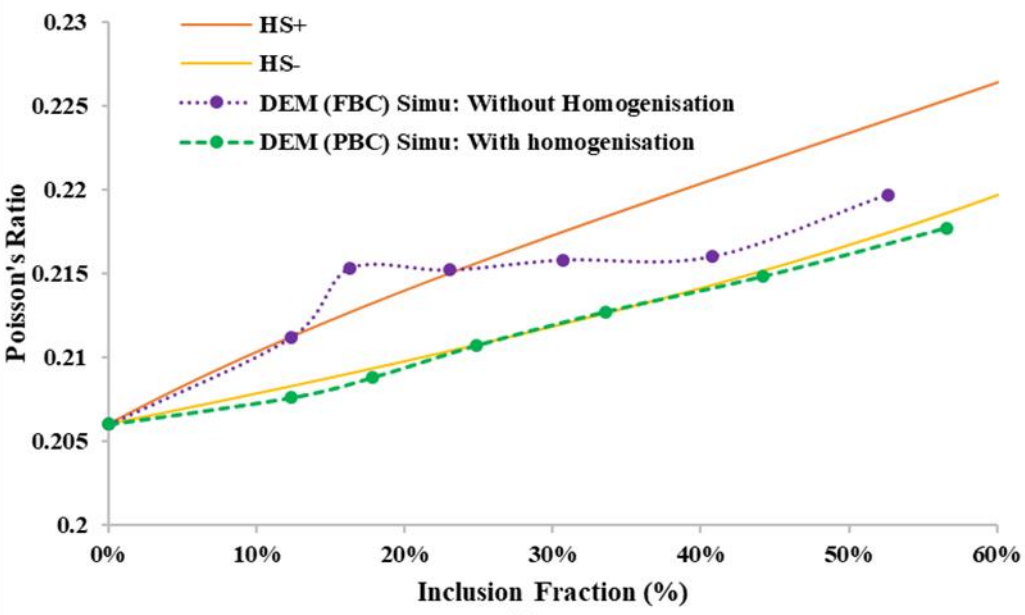
The first comparison for this study is to ensure the efficiency and the accuracy of the homogenization technique on the prediction of apparent elastic properties. In this aim, the results obtained by PBC are compared to the Free Boundary Condition (FBC), which is without any homogenization. As mentioned in section 4.1.2, the apparent elastic properties should follow:

- the lower HS- bound in the case of G/A two-phase material;
- the upper HS+ bound in the case of G/P porous material.

Fig. 11 (a) and (b) are showing the simulation results of the apparent Young's modulus ( $E^{ap}$ ) and Poisson's ratio ( $\nu^{ap}$ ) for the different considered volume fractions of inclusions. The analytical Hashin and Shtrikman (HS) bounds have been calculated and plotted for comparison.



(a)



(b)

Fig. 11. Comparison of PBC and FBC for (a) apparent Young's modulus ( $E^{ap}$ ) and (b) Poisson's ratio ( $\nu^{ap}$ ) in the case of G/A two-phase materials

As shown in Fig. 11 (a), the FBC model starts to deviate from the HS- lower bound, especially for high volume fractions of inclusion (higher than 25%). This deviation tends to the middle range of the HS bounds, which is in line with previous studies by another DEM code, GranOO<sup>1</sup>, which used randomly distributed inclusions [53]. However, the model with the periodic homogenization, which is used for this study, was in accordance with the theoretical HS- lower bound.

<sup>1</sup> <https://www.granoo.org/>

As it was shown in Fig. 11 (b), the apparent Poisson's ratio ( $\nu^{ap}$ ) simulations with the periodic homogenization are closely following the lower bound (HS-) while the model without homogenization is not following HS bounds. Additionally, these FBC apparent Poisson's ratio results exhibit some irregularities. To explain this inaccuracy with FBC, it should be mentioned that, for measuring the apparent Poisson's ratio ( $\nu^{ap}$ ) in the simulations, uniform tensile displacements were applied on one of the main axes of the sample, and the strains were measured on the faces in perpendicular directions (for which some roughness could come from the spatial distribution of discrete elements). Nevertheless, a uniform strain hypothesis was used to compute the apparent Poisson's ratio. This hypothesis remains questionable and may lead to these significant discrepancies. In the case of PBC, since the boundaries remain planar, this problem does not exist.

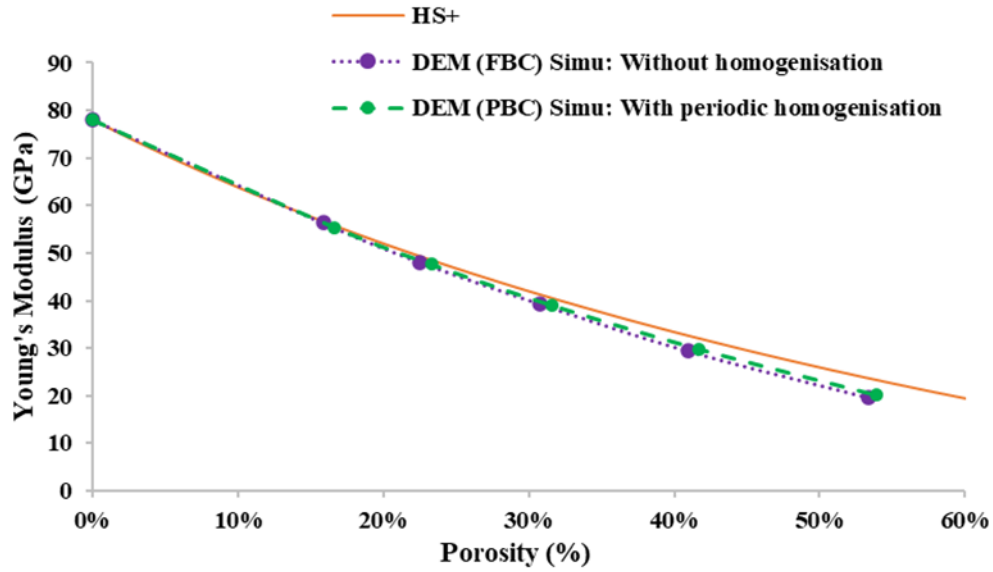
To compare quantitatively FBC and PBC, the relative deviation of Young's modulus ( $E_{error}$ ) and Poisson's ratio ( $\nu_{error}$ ) from the HS- bound for each simulation has been calculated as follows:

$$E_{error} = \frac{|E_{simu} - E_{HS-}|}{E_{HS-}} \quad \text{Eq. 5}$$

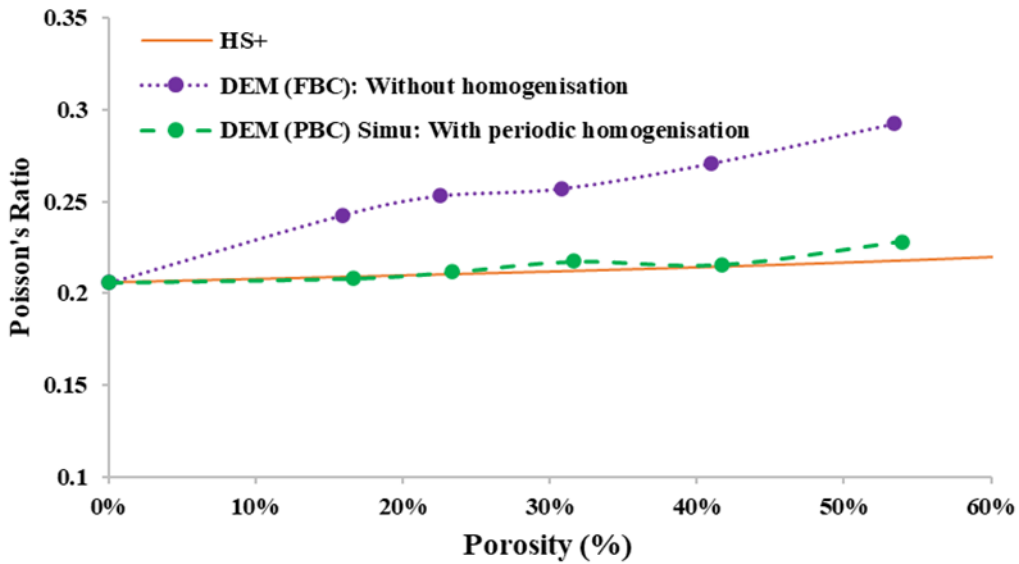
$$\nu_{error} = \frac{|\nu_{simu} - \nu_{HS-}|}{\nu_{HS-}} \quad \text{Eq. 6}$$

Then by having relative deviation for each simulated inclusion fraction, the mean deviations for PBC and FBC were calculated. The mean deviation of Young's modulus for the PBC model was 0.3% (min 0 % and max 0.7%), while for the FBC, it was 1.4% (min 0% and max 4.9%). In addition, the mean deviation for Poisson's ratio for the PBC was 0.2% (min 0% and max 0.4%) while for the FBC, it was 1.5% (min 0% and max 3.0%).

Similar investigations were managed for the case of G/P porous material. Fig. 12 (a) and (b) are showing the simulation results of the apparent Young's modulus ( $E^{ap}$ ) and Poisson's ratio ( $\nu^{ap}$ ) for the different considered porosities, in this case. The analytical Hashin and Shtrikman (HS) bounds have also been calculated and plotted for comparison.



(a)



(b)

Fig. 12. Comparison of PBC and FBC for (a) apparent Young's modulus ( $E^{ap}$ ) and (b) Poisson's ratio ( $\nu^{ap}$ ) in the case of G/P porous materials.

As it is shown in Fig. 12 (a), for the case of porous materials G/P, the FBC model tends again to deviate from the HS+ analytical reference for Young's modulus, while the PBC model shows a better agreement, as previously.

In the same way, in Fig. 12 (b), the FBC model is progressively deviating from the HS+ analytical reference for Poisson's ratio, while the PBC follows the upper bound (HS+) with good accordance. However, in the case of porous materials, these FBC discrepancies for Poisson's ratio are more significant, probably due to higher contrast between the elastic properties of matrix and pores.

Again, to quantitatively compare FBC and PBC, the relative deviations from the HS+ bound have been calculated in the same way.

The mean relative deviation  $E_{error}$  for the PBC model was 4.5% (min 0% and max 13.9%), while for the FBC model, it was 5.8% (min 0% and max 17.3%). The mean relative deviation  $\nu_{error}$  for the PBC model was 4.9% (min 0% and max 12.0%) while for the FBC model, it was 24.1% (min 0% and max 43.6%).

Overall, this study demonstrates that DEM models using periodic homogenization exhibit much better agreement with the analytical HS bounds for both two-phase and porous materials than using free boundary conditions. This study highlights the interest in using PBC for predicting apparent elastic properties of multiphase material within the DEM frameworks.

#### 4.2.2 Number of discrete elements

In this section, the number of discrete elements to build an RVE is discussed. The primary motivation of using the presented homogenization technique is to scale up the behavior of the materials from micro to macro scale. This means that the apparent properties of a heterogeneous material could be reproduced by only simulating a small fraction of the whole specimen. Compared to FEM, this advantage is even more tangible due to the high calculation cost of DEM simulations. In DEM, an infinite heterogeneous media could be reproduced by a relatively small number of discrete elements in RVEs combined with PBC. However, even in building an RVE, the number of discrete elements could be influential. To study this influence, FCC-arranged RVEs have been produced with approximately 20k discrete elements, as shown in Fig. 13 (a), and compared to 68k discrete elements as shown in Fig. 13 (b). It is worth mentioning that the input parameters of 20k and 68k samples were calibrated separately. However, the calibrated input values were relatively close.

For 20k discrete elements, the calculation time for each simulation took about 8 to 10 minutes. For 68k discrete elements, the calculation time for each simulation took an average of 6 to 7 times longer than 20k (both on a system with Intel Core Xeon E2186M 4.0 GHz, SSD, 16 GB RAM, 12 parallel threads). The results of simulations for different numbers of DEs (20k and 68k) are plotted in Fig. 14.

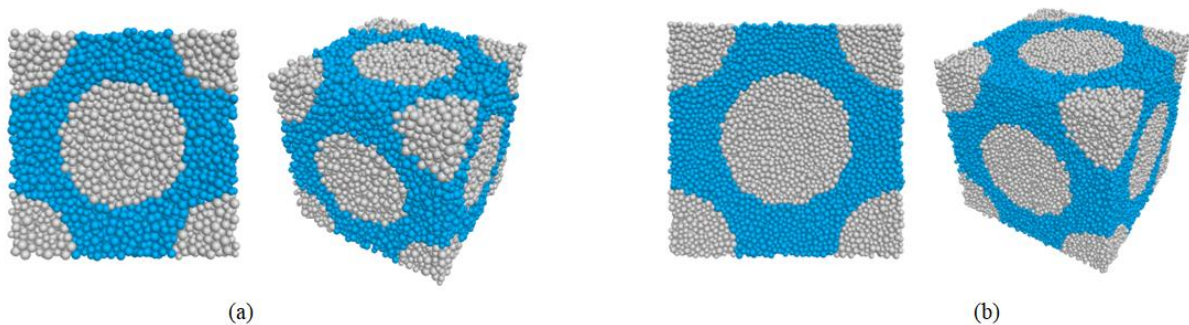
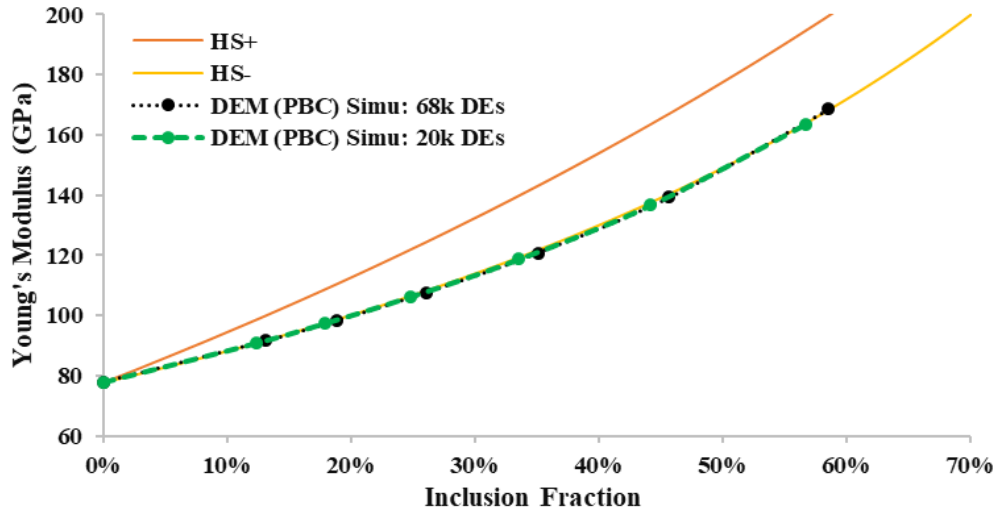
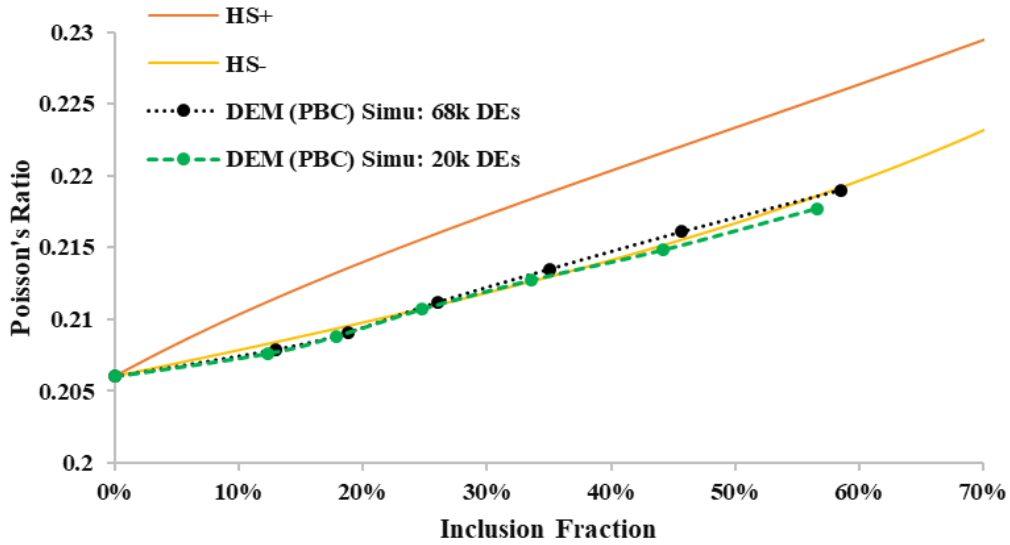


Fig. 13. RVEs with the different number of DEs and fineness:  
(a) 20k discrete elements and (b) 68k discrete elements



(a)



(b)

Fig. 14. Comparison of 20k and 68k RVEs with PBC for G/A two-phase material: (a) apparent Young's modulus ( $E^{ap}$ ) and (b) apparent Poisson's ratio ( $\nu^{ap}$ ).

As shown in Fig. 14 (a), the relative deviation from Young's modulus HS- lower bound is less than 1.0% for both 20k and 68k RVEs. Also, as shown in Fig. 14 (b), the relative deviation from Poisson's ratio HS- lower bound is less than 0.4% for both RVEs. By considering these deviations, both models exhibit a very similar high accuracy in representing the apparent elastic behavior of two-phase materials. This means, by having the same relative accuracy, the model with 20k DEs is more efficient in terms of calculation performance. It emphasizes that, even with a relatively low number of DEs (20k DEs), the model is giving a valid response for the apparent elastic behavior. These results demonstrate the importance of using periodic homogenization for decreasing the computation time and cost by decreasing the number of DEs and the fineness of the models. It is a critical point in DEM models, where calculation efficiency is much more demanding in comparison to the other numerical methods. For this reason, the RVEs with 20k DEs considering PBC was mainly used in the present study.

### 4.2.3 Inclusion fraction calculation

As mentioned in section 4.1.2, for positioning and comparing the simulated results of the apparent elastic properties of two-phase or porous materials on the HS bounds diagrams, one of the influential parameters is the inclusion fraction. For precisely calculating the inclusion fractions of the simulated FCC arrangements of RVEs, two approaches were investigated. Firstly, it was calculated based on the volume of the DEs in each part (matrix and inclusion) as follows:

$$f_i^V = \frac{\sum V_{inclu}^{DE}}{\sum V_{inclu}^{DE} + \sum V_{matrix}^{DE}} \quad \text{Eq. 7}$$

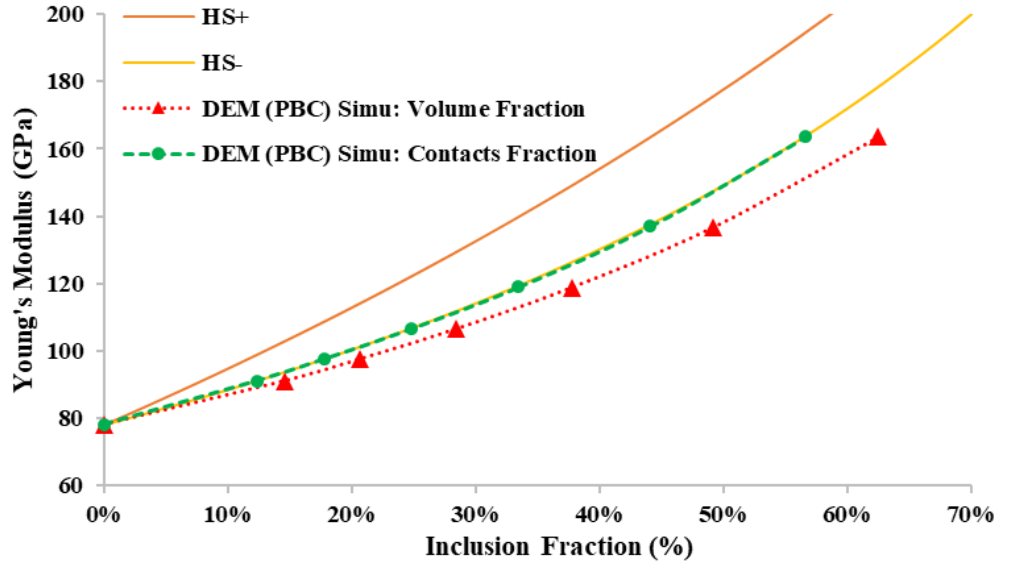
where  $f_i^V$  is the inclusion fraction calculated by volume fraction,  $\sum V_{inclu}^{DE}$  is the total volume of DEs within the inclusions, and  $\sum V_{matrix}^{DE}$  is the total volume of DEs within the matrix. With this formulation, the porosity between the DEs is supposed to be the same in the inclusions and in the matrix, allowing to simplify the porosity term from each.

The second approach calculates the inclusion fraction by the relative number of the contacts in each part of the material. This means the total number of contacts within the inclusions over the total number of existing contacts (Eq. 8). Note that as mentioned in section 3.2, the matrix-inclusion interface contacts were considered as a matrix-matrix contact. Therefore, the proposed inclusion fraction calculation is:

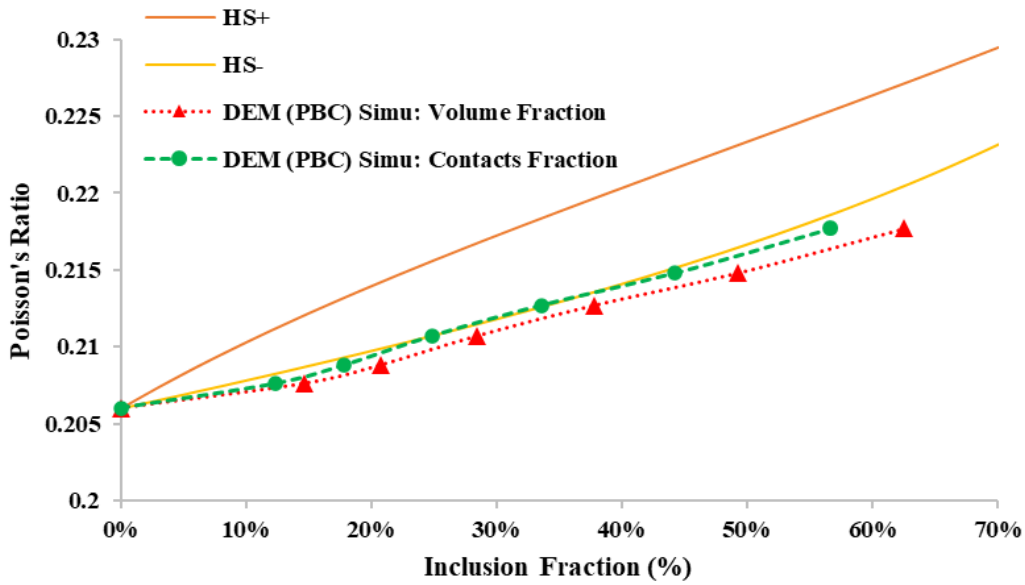
$$f_i^C = \frac{N_{inclu}^C}{N_{inclu}^C + N_{matrix}^C} \quad \text{Eq. 8}$$

where  $f_i^C$  is the inclusion fraction calculated by the number of contacts,  $N_{inclu}^C$  is the total number of contacts within the inclusions, and  $N_{matrix}^C$  is the total number of contacts within the matrix (including the interface contacts).

In Fig. 15, the comparison and the accuracy of these two methods have been compared regarding the HS bounds.



(a)



(b)

Fig. 15. Comparison of DEs volume fraction and contact fraction approaches for calculating inclusion fractions: (a) apparent Young's modulus ( $E^{ap}$ ) and (b) apparent Poisson's ratio ( $\nu^{ap}$ ).

As shown in Fig. 15, the calculation of the inclusion fraction by contacts is much closer to the HS- reference bound. The average deviation from HS- bound for the positioning of the apparent Young's modulus ( $E^{ap}$ ) by using contacts number is 0.3% (min 0% and max 0.7%) while this deviation reaches up to 4.7% (min 0% and max 8.4%) for the volume fraction approach. In the same way, for the apparent Poisson's ratio ( $\nu^{ap}$ ), this deviation for contacts number approach is 0.2% (min 0% and max 0.4%) while this deviation reaches up to for 2.6% (min 0% and max 4.2%) for the volume fraction approach.

At first sight, this better accuracy of the contacts number approach could appear surprising. However, it should be highlighted that in DEM, the apparent materials properties are coming from the responses of the contacts and not from the discrete elements themselves since they are considered as rigid bodies. Hence, it is logical that in DEM, the most pertinent parameter to

account for the experimental inclusion volume fraction is the contact number (and not the volume of the elements).

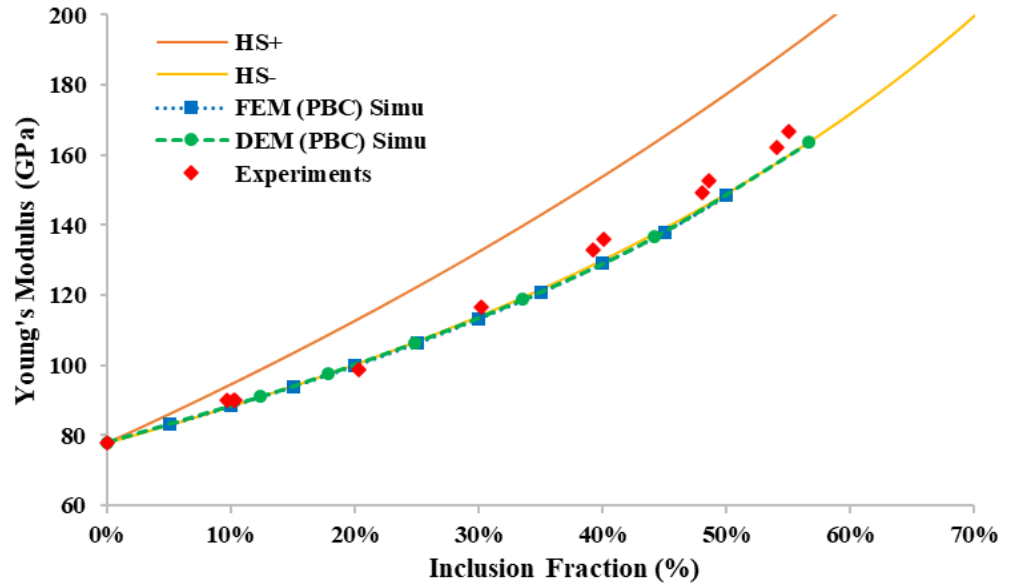
By considering the mentioned results in Fig. 15, the contacts number approach was chosen later to calculate the inclusions fraction in the periodic homogenization of DEM models. Regarding the porosity percentage calculation in the DEM models, this approach was used by simply replacing the total number of the inclusion contacts ( $N_{\text{inclu}}^C$ ) with the total number of the deleted contacts during the building procedure of porous material RVEs.

### **4.3 Young's modulus and Poisson's ratio obtained by DEM using PBC confronted with reference values**

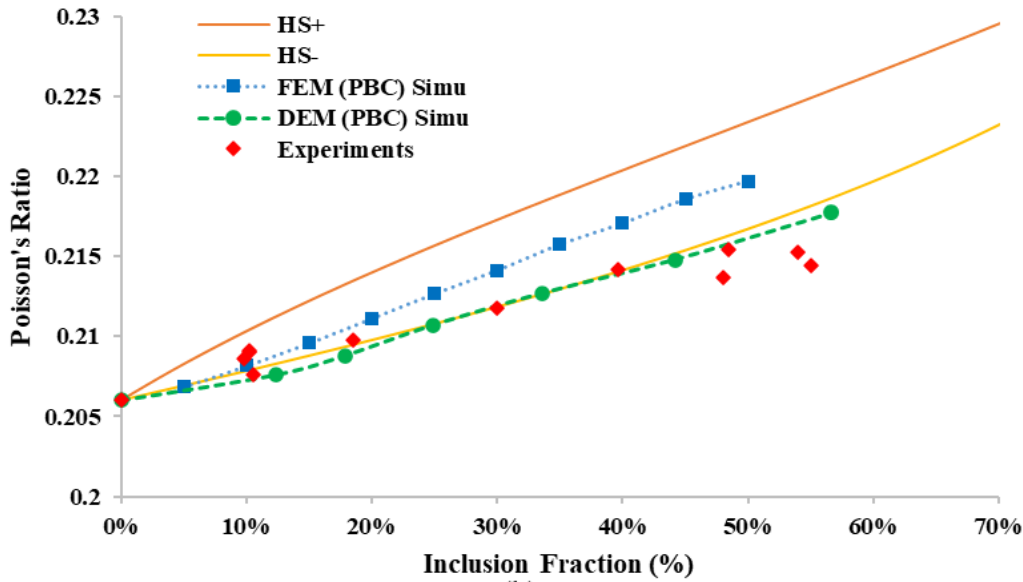
To quantitatively ensure the validity of the proposed DEM model, the obtained results using the periodic homogenization have been confronted with the other reference values coming from experimental measurements, analytical approaches, and FEM calculations.

#### **4.3.1 Case 1: Stiffer inclusions**

In this section, the results of the simulation of the model material with stiffer inclusions (glass matrix with alumina spherical inclusions G/A) have been investigated. As mentioned before, theoretically, by increasing the inclusion fraction in the RVEs, the results should follow the lower HS bound (HS-) [47] [49] [48]. Therefore, the inclusion fraction in the DEM model RVEs increased as well as in the FEM model and then compared to the experimental reference values. Besides, both DEM and FEM models used RVEs in the FCC arrangement with periodic homogenization.



(a)



(b)

Fig. 16. DEM periodic homogenization results confronted to HS bounds, FEM models, and real experimental data: (a) apparent Young's modulus ( $E^{ap}$ ) and (b) apparent Poisson's ratio ( $\nu^{ap}$ ).

As it can be seen in Fig. 16 (a), the DEM simulation using PBC and FEM periodic homogenization are in perfect accordance with HS lower bound (HS-). Also, the experimental points are following the HS lower bound too, but with a slight tendency to the middle range of HS bounds for the higher inclusion fractions.

Regarding Fig. 16 (b), although the HS bounds width was small (values between 0.2 and 0.23), the DEM model exhibits better accordance with reference HS- bound for predicting the apparent Poisson's ratio, which is more coherent with the experimental results as well.

A summary of the relative deviation of DEM using PBC, DEM using FBC, and FEM using PBC from HS- is shown in Table 5.

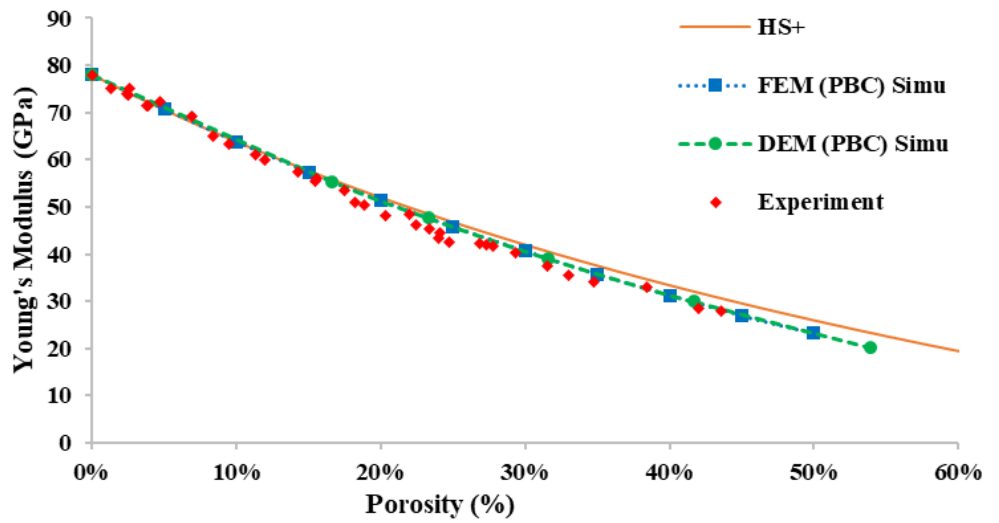
Table 5. Summary of the relative deviations from HS- reference bound for DEM using PBC, DEM using FBC, and FEM using PBC

Method	Deviation of apparent Young's modulus from HS-			Deviation of apparent Poisson's ratio from HS-		
	Minimum	Maximum	Average	Minimum	Maximum	Average
<b>FEM PBC</b>	0.03%	0.91%	0.55%	0.02%	1.49%	0.88%
<b>DEM PBC</b>	0.00%	0.73%	0.29%	0.00%	0.42%	0.17%
<b>DEM FBC</b>	0.00%	4.91%	1.44%	0.00%	3.01%	1.48%

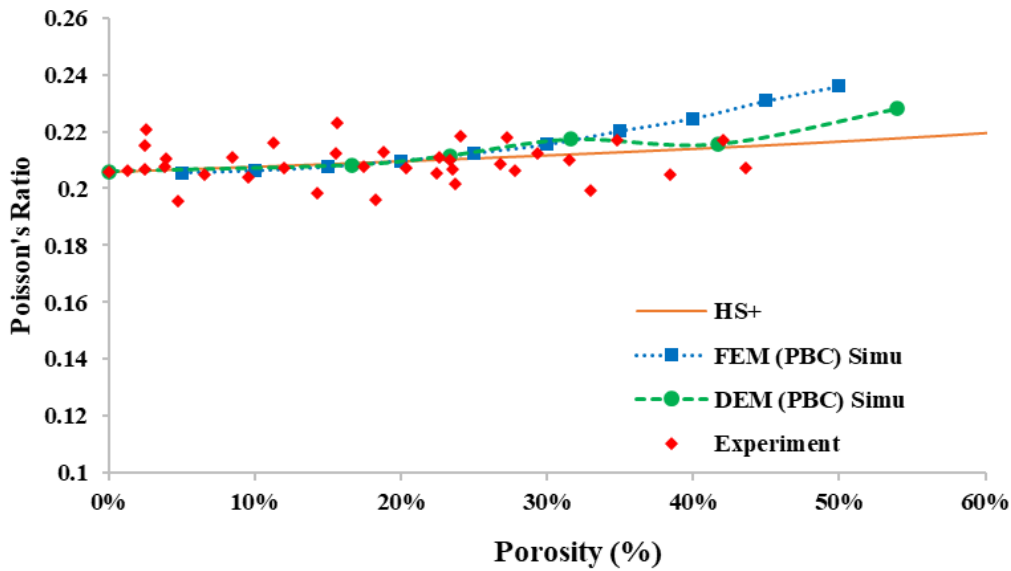
Considering Table 5 for both apparent elastic parameters, the DEM model shows a smaller deviation compared to the FEM model, either mean or maximum values, especially for modeling the apparent Poisson's ratio. These results highlight the potential of DEM for solving multiscale problems by using periodic homogenization.

### 4.3.2 Case 2: Porosity effect

In this section, the effect of porosity has been studied (glass matrix with spherical pores G/P). In this case, as mentioned in section 4.1.2, the HS upper bound (HS+) will be the analytical reference for the porous material G/P, whereas HS lower bound (HS-) is zero [50] [51] [52].



(a)



(b)

Fig. 17. DEM periodic homogenization results confronted to HS bounds, FEM models, and real experimental data: (a) apparent Young's modulus ( $E^{ap}$ ) and (b) apparent Poisson's ratio ( $\nu^{ap}$ ).

As shown in Fig. 17 (a), both DEM and FEM periodic homogenizations are in perfect accordance with the lower inclusion fraction values (up to 30%). It exhibits an increasingly small difference for higher values. On the other hand, both simulation results match with the tendency of the experimental values considering the discrepancy of measurements.

In Fig. 17 (b), the DEM model shows better accordance with HS upper bound (HS+) globally compared to the FEM model for apparent Poisson's ratio, which confirms the results of the previous section. However, both models started to deviate from HS+ for high porosities (above 35% for FEM and above 45% for DEM). Despite the discrepancy of the experimental measurements (fluctuating in the range of 0.19 to 0.22 around the HS+) and the slight deviation for high porosity, both FEM and DEM exhibit good accordance with experimental results. A

summary of the relative deviation of DEM using PBC, DEM using FBC, and FEM using PBC from HS+ is shown in Table 6.

Table 6. Summary of the relative deviations from HS+ reference bound for DEM using PBC, DEM using FBC, and FEM using PBC

Method	Deviation of apparent Young's modulus from HS+			Deviation of apparent Poisson's ratio from HS+		
	Minimum	Maximum	Average	Minimum	Maximum	Average
<b>FEM PBC</b>	0.00%	11.23%	3.99%	0.05%	15.85%	6.06%
<b>DEM PBC</b>	0.00%	13.88%	4.54%	0.00%	12.05%	4.87%
<b>DEM FBC</b>	0.00%	17.25%	5.84%	0.00%	43.64%	24.06%

Simulation of the porous media by using DEM periodic homogenization results shows matching values with FEM simulations and experimental results. Hence, even if FEM modeling is well-known to predict elastic properties of porous materials [54], the DEM modeling with PBC can also be used to predict accurately such homogenized elastic properties. To verify further the proposed DEM approach, the stiffness tensors calculation will be discussed in the following section.

## 4.4 Stiffness tensors investigations

In this section, the apparent stiffness tensors given by DEM RVEs are investigated. As a first step, the potential anisotropy of the equivalent modeled media is discussed. To do so, the DEM model stiffness tensors were calculated by cubic and orthotropic symmetry assumptions (see section 3.7). Then, the stiffness tensors obtained by DEM are compared to the reference values coming from the HS relationships and the FEM model. To be able to compare the values, the inclusion fraction of 50% for the RVEs was chosen as the comparison reference for all the cases.

### 4.4.1 Stiffness tensors obtained by cubic and orthotropic symmetry assumptions

As previously explained for calculating the RVEs stiffness tensor in the DEM model, two different approaches were used: calculating the RVEs stiffness tensors by cubic symmetry assumption from Eq. 3 and orthotropic symmetry assumption from Eq. 4. A comparison was made between these two assumptions to reveal any potential influence of the random spatial positioning of discrete elements in RVEs, which could lead to a certain level of mechanical anisotropy coming from this asymmetry. The numerical steps for calculating the stiffness tensors in DEM by using PBC and distortion of the boundaries have been explained in section 3.7. The resulting stiffness tensors are given below:

$$C_{ij} = \begin{pmatrix} 168.8 & 46.6 & 46.6 & 0 & 0 & 0 \\ & 168.8 & 46.6 & 0 & 0 & 0 \\ & & 168.8 & 0 & 0 & 0 \\ Sym & & & 65.5 & 0 & 0 \\ & & & 0 & 65.5 & 0 \\ & & & 0 & 0 & 65.5 \end{pmatrix} \quad C_{ij} = \begin{pmatrix} 168.7 & 46.6 & 46.3 & 0 & 0 & 0 \\ & 168.5 & 46.3 & 0 & 0 & 0 \\ & & 168.4 & 0 & 0 & 0 \\ Sym & & & 65.5 & 0 & 0 \\ & & & 0 & 65.4 & 0 \\ & & & 0 & 0 & 65.7 \end{pmatrix}$$

(a) (b)

Fig. 18. Stiffness tensors for DEM model in the case of the G/A with 50% inclusion: (a) cubic symmetry assumption, (b) orthotropic symmetry assumption.

In order to compare these two stiffness tensors, the HS- reference will be used. By knowing the elastic properties of the constituents, the HS- bound elastic properties can be calculated. Finally, from these properties and considering an isotropic assumption, the stiffness tensor for the reference HS- is obtained as bellow:

$$C_{ij} = \begin{pmatrix} 169.5 & 46.9 & 46.9 & 0 & 0 & 0 \\ & 169.5 & 46.9 & 0 & 0 & 0 \\ & & 169.5 & 0 & 0 & 0 \\ Sym & & & 61.3 & 0 & 0 \\ & & & 0 & 61.3 & 0 \\ & & & 0 & 0 & 61.3 \end{pmatrix}$$

Fig. 19. Stiffness tensors for the G/A model two-phase material with 50% inclusion calculated for the reference HS-.

Afterward, to compare to the reference HS-, the differences of  $C_{ij}$  matrices for the DEM using cubic and orthotropic assumptions with the reference tensor have been calculated:

$$\Delta C_{ij} = \begin{pmatrix} -0.7 & -0.3 & -0.3 & 0 & 0 & 0 \\ & -0.7 & -0.3 & 0 & 0 & 0 \\ & & -0.7 & 0 & 0 & 0 \\ Sym & & & 4.2 & 0 & 0 \\ & & & 0 & 4.2 & 0 \\ & & & 0 & 0 & 4.2 \end{pmatrix} \quad \Delta C_{ij} = \begin{pmatrix} -0.8 & -0.3 & -0.3 & 0 & 0 & 0 \\ & -1 & -0.3 & 0 & 0 & 0 \\ & & -1.1 & 0 & 0 & 0 \\ Sym & & & 4.2 & 0 & 0 \\ & & & 0 & 4.1 & 0 \\ & & & 0 & 0 & 4.4 \end{pmatrix}$$

(a) (b)

Fig. 20. Differences matrices to HS- bound for DEM model: (a) cubic symmetry assumption (b) orthotropic symmetry assumption.

Considering different approaches in the DEM model for calculating the stiffness tensors, as shown in Fig. 20 (a) and (b), the obtained stiffness tensors for both assumptions are in accordance. The errors between cubic symmetry tensors and the orthotropic tensors for:

- the main diagonal elements  $C_{11}$ ,  $C_{22}$ ,  $C_{33}$ , was less than 0.2%,
- the main diagonal elements  $C_{44}$ ,  $C_{55}$ ,  $C_{66}$ , was less than 0.5% and
- the off-diagonal elements  $C_{12}$ ,  $C_{13}$ ,  $C_{23}$ , was less than 0.6%.

These results show that the random spatial positioning of discrete elements in RVEs had a minimal impact on the anisotropy of the RVE, even with a relatively low number of DEs for RVEs. It has shown the sufficiency of 20k DEs for RVEs in the PBC, and yet validating the efficiency of using periodic homogenization in DEM, for saving calculation time and resources.

#### 4.4.2 Stiffness tensors obtained by DEM using PBC confronted with reference values

Here, the obtained values for the stiffness tensor of the DEM model are compared to the reference values coming from the HS- bound (in Fig. 19) and FEM numerical model. The obtained stiffness tensors results are shown below:

$$C_{ij} = \begin{pmatrix} 168.8 & 46.6 & 46.6 & 0 & 0 & 0 \\ & 168.8 & 46.6 & 0 & 0 & 0 \\ & & 168.8 & 0 & 0 & 0 \\ & Sym & & 65.5 & 0 & 0 \\ & & & 0 & 65.5 & 0 \\ & & & 0 & 0 & 65.5 \end{pmatrix} \quad C_{ij} = \begin{pmatrix} 169.3 & 47.7 & 47.7 & 0 & 0 & 0 \\ & 169.3 & 47.7 & 0 & 0 & 0 \\ & & 169.3 & 0 & 0 & 0 \\ & Sym & & 63.5 & 0 & 0 \\ & & & 0 & 63.5 & 0 \\ & & & 0 & 0 & 63.5 \end{pmatrix}$$

(a)
(b)

Fig. 21. Stiffness tensors for the G/A model two-phase material with 50% inclusion calculated for (a) the DEM model, (b) the FEM model. FEM results from [4]

Considering the stiffness tensors obtained by DEM (Fig. 21 (a)) and FEM (Fig. 21 (b)) and comparing these values with HS- reference, both numerical methods are having good accordance with HS-.

For the first three diagonal components ( $C_{11}$ ,  $C_{22}$ ,  $C_{33}$ ), DEM and FEM models had excellent accordance with HS-, by having 0.4% and 0.1% of errors, respectively. For the last three diagonal components ( $C_{44}$ ,  $C_{55}$ ,  $C_{66}$ ), the FEM model showed a better agreement with HS- compared to the DEM model by having 3.6% error while the DEM model error was 6.8%. Finally, the three off-diagonal components ( $C_{12}$ ,  $C_{13}$ ,  $C_{23}$ ) in the DEM model showed better accordance with HS- by having 0.6% error while the FEM model has 1.7% error.

Overall, the material stiffness tensor matrix, obtained by the DEM model and using PBC, showed excellent accordance with HS- values and the FEM model. It verifies the accuracy and efficiency of DEM models with periodic homogenization to predict the elastic properties and stiffness coefficients of two-phase material.

## 5 Conclusions

In this paper, the elastic properties of model two-phase and porous materials were accurately simulated by using a DEM numerical approach combined with a periodic homogenization method. In fact, the homogenization technique is usually a key point for multiscale modeling and reducing calculation times. Well-known in FEM, this approach is much less developed in DEM for continuum media. The proposed method and the associated algorithm procedures constitute a promising route for a better understanding of the thermomechanical behavior of ceramics. The first results presented here, only about elastic behavior in non-damaged materials, validate the DEM efficiency and demonstrate its accuracy for homogenization and up-scaling problems for two-phase and porous model materials. Also, this study highlights the importance of using periodic boundaries instead of free boundary conditions.

The DEM periodic homogenization simulation outputs, which were used to predict and scale up the elastic behavior of two-phase and porous model materials, were compared and were validated thanks to excellent accordance with experimental results as well as other predictive analytical and numerical methods:

- I. Experimental results: regarding the elastic behavior of real model material with Alumina inclusions, the DEM simulations exhibit very good accordance with both Young's modulus and Poisson's ratio values versus the different percentage of inclusions. In the case of the elastic behavior of real porous model material, the DEM simulations also exhibit very good accordance for Young's modulus values versus porosity. About Poisson's ratio, although the experimental results were a bit scattered, the DEM predictions were still in acceptable accordance with experimental values.
- II. Hashin and Shtrikman bounds: for both the DEM models, either the two-phase material with Alumina inclusions and the porous model, Young's modulus and Poisson's ratio values exhibit excellent accordance with the HS bounds (HS- in the case of alumina inclusions and HS+ in the case of porous materials). This confirms the results of other related studies about the elastic behavior of two-phase materials with stiff inclusions in a soft matrix [47] [49] [48] and porous materials [3].
- III. FEM simulation: comparison between FEM and DEM for simulating the same two-phase and porous materials demonstrates that the DEM approach leads to closer predictions for the elastic properties (considering both experimental and analytical values as reference) in comparison to the FEM simulations. It was especially the case for Poisson's ratio in two-phase and porous materials. In fact, in this case, the DEM approach seems to exhibit better accordance with the HS lower bound.

Later, the stiffness tensor ( $C_{ij}$ ) of each analytical (calculated from HS- values), FEM, and DEM methods were calculated and compared. It appears that DEM and FEM results exhibit an acceptable agreement with the stiffness tensor calculated from analytical HS- values. However, the FEM model showed a bit better accuracy in predicting the shear stiffness than the DEM model. At this stage, the reason for the better prediction of FEM in the shear stiffness requires further dedicated studies.

The main limitation of the present study was the time-consuming trial-and-error process for calibrating the DEM input parameters to reproduce the apparent properties of real materials. Nevertheless, this well-known drawback in DEM could be later overcome by an automated calibration process, for example, using a machine learning approach.

Overall, the proposed DEM approach, combined with the periodic homogenization technique, leads to valid elastic properties determination for two-phase and porous model materials. These key results open very interesting new ways to use DEM to predict the thermomechanical behavior of heterogeneous ceramics containing numerous microcracks that could propagate simultaneously. In fact, the fracturing process and microcracking simulations are one of the key interests of using DEM in such a case compared to FEM. Therefore, further steps will simulate a simultaneous microcracking that could be induced by the thermal expansion mismatch between the ceramic's constituents. This technique can thus be used to optimize the microstructure of refractory ceramics, aiming to improve their thermal shock resistance.

## 6 Acknowledgment

This work was supported by the funding scheme of the European Commission, Marie Skłodowska-Curie Actions Innovative European Training Networks in the frame of the project ATHOR (Advanced THERmomechanical multiscale mODElling of Refractory linings) Grant No. 764987. Also, this research was supported by The Journal of the European Ceramic Society

(JECS) through the JECS Trust scholarship scheme under contract No. 2018188. Moreover, this work was done in partnership with the ITASCA consulting group, in the frame of ITASCA Educational Partnership (IEP), and the authors would like to express their sincere gratitude for their support and provide the PFC software. Finally, the authors would like to express their gratitude to Dr. Nicolas Tessier-Doyen and Dr. Renaud Grasset-Bourdel for providing experimental and FEM outputs, respectively, to validate the proposed DEM approach.

## 7 References

- [1] Z. Hashin, ‘The Elastic Moduli of Heterogeneous Materials’, *J. Appl. Mech.*, vol. 29, no. 1, pp. 143–150, Mar. 1962, doi: 10.1115/1.3636446.
- [2] Z. Hashin and S. Shtrikman, ‘A variational approach to the theory of the elastic behaviour of multiphase materials’, *Journal of the Mechanics and Physics of Solids*, vol. 11, no. 2, pp. 127–140, Mar. 1963, doi: 10.1016/0022-5096(63)90060-7.
- [3] O. Zerhouni, M. G. Tarantino, and K. Danas, ‘Numerically-aided 3D printed random isotropic porous materials approaching the Hashin-Shtrikman bounds’, *Composites Part B: Engineering*, vol. 156, pp. 344–354, Jan. 2019, doi: 10.1016/j.compositesb.2018.08.032.
- [4] R. Grasset-Bourdel *et al.*, ‘Optimisation of 3D RVE for anisotropy index reduction in modelling thermoelastic properties of two-phase composites using a periodic homogenisation method’, *Computational Materials Science*, vol. 50, no. 11, pp. 3136–3144, Oct. 2011, doi: 10.1016/j.commatsci.2011.05.042.
- [5] N. Tessier-Doyen, ‘Etude expérimentale et numérique du comportement thermomécanique de matériaux réfractaires modèles’, thesis, University of Limoges, Limoges, France, 2003. Accessed: Apr. 28, 2020. [Online]. Available: <http://www.theses.fr/2003LIMO0030>
- [6] N. Tessier-Doyen, J. C. Glandus, and M. Huger, ‘Experimental and numerical study of elastic behavior of heterogeneous model materials with spherical inclusions’, *J Mater Sci*, vol. 42, no. 14, pp. 5826–5834, Jul. 2007, doi: 10.1007/s10853-006-1386-8.
- [7] I. Babuška, B. Andersson, B. Guo, J. M. Melenk, and H. S. Oh, ‘Finite element method for solving problems with singular solutions’, *Journal of Computational and Applied Mathematics*, vol. 74, no. 1, pp. 51–70, Nov. 1996, doi: 10.1016/0377-0427(96)00017-9.
- [8] P. A. Cundall, ‘A computer model for simulating progressive, large-scale movements in blocky rock systems’, 1971.
- [9] G. A. D’Addetta, F. Kun, and E. Ramm, ‘On the application of a discrete model to the fracture process of cohesive granular materials’, *GM*, vol. 4, no. 2, pp. 77–90, Jul. 2002, doi: 10.1007/s10035-002-0103-9.
- [10] F. Asadi, D. André, S. Emam, P. Doumalin, I. Khlifi, and M. Huger, ‘Investigation of different discrete modeling strategies to mimic microstructural aspects that influence the fracture energy of refractory materials’, *Open Ceramics*, vol. 11, p. 100288, Sep. 2022, doi: 10.1016/j.oceram.2022.100288.
- [11] L. Scholtès and F.-V. Donzé, ‘Modelling progressive failure in fractured rock masses using a 3D discrete element method’, *International Journal of Rock Mechanics and Mining Sciences*, vol. 52, pp. 18–30, Jun. 2012, doi: 10.1016/j.ijrmms.2012.02.009.
- [12] B. Pulatsu, E. Erdogmus, P. B. Lourenço, J. V. Lemos, and J. Hazzard, ‘Discontinuum analysis of the fracture mechanism in masonry prisms and wallettes via discrete element

- method', *Meccanica*, vol. 55, no. 3, pp. 505–523, Mar. 2020, doi: 10.1007/s11012-020-01133-1.
- [13] D. Potyondy and P. A. Cundall, 'A bonded-particle model for rock', *International Journal of Rock Mechanics and Mining Sciences*, vol. 41, no. 8, pp. 1329–1364, Dec. 2004, doi: 10.1016/j.ijrmms.2004.09.011.
- [14] D. Potyondy, 'Simulating perforation damage with a flat-jointed bonded-particle material', presented at the 51st U.S. Rock Mechanics/Geomechanics Symposium, Aug. 2017. Accessed: Apr. 28, 2020. [Online]. Available: <https://www.onepetro.org/conference-paper/ARMA-2017-0223>
- [15] F. Asadi, D. André, S. Emam, P. Doumalin, and M. Huger, 'Numerical Modelling of The Quasi-Brittle Behaviour of Refractory Ceramics by Considering Microcracks Effect', *Journal of the European Ceramic Society*, Nov. 2021, doi: 10.1016/j.jeurceramsoc.2021.11.016.
- [16] F. Asadi, 'Micro-mechanical modelling of heterogeneous materials containing microcracks with Discrete Element Method (DEM)', Doctoral dissertation, Limoges, 2021. Accessed: Nov. 13, 2021. [Online]. Available: <http://www.theses.fr/2021LIMO0046>
- [17] M. Parrinello and A. Rahman, 'Polymorphic transitions in single crystals: A new molecular dynamics method', *Journal of Applied Physics*, vol. 52, no. 12, pp. 7182–7190, Dec. 1981, doi: 10.1063/1.328693.
- [18] M. Huger, T. Ota, N. Tessier-Doyen, P. Michaud, and T. Chotard, 'Microstructural effects associated to CTE mismatch for enhancing the thermal shock resistance of refractories', *IOP Conf. Ser.: Mater. Sci. Eng.*, vol. 18, no. 22, p. 222002, Sep. 2011, doi: 10.1088/1757-899X/18/22/222002.
- [19] T. Belytschko and T. Black, 'Elastic crack growth in finite elements with minimal remeshing', *International Journal for Numerical Methods in Engineering*, vol. 45, no. 5, pp. 601–620, 1999, doi: 10.1002/(SICI)1097-0207(19990620).
- [20] T. Belytschko, N. Moës, S. Usui, and C. Parimi, 'Arbitrary discontinuities in finite elements', *International Journal for Numerical Methods in Engineering*, vol. 50, no. 4, pp. 993–1013, 2001, doi: 10.1002/1097-0207(20010210).
- [21] N. Moës, J. Dolbow, and T. Belytschko, 'A finite element method for crack growth without remeshing', *International Journal for Numerical Methods in Engineering*, vol. 46, no. 1, pp. 131–150, 1999, doi: 10.1002/(SICI)1097-0207(19990910).
- [22] F. V. Souza and D. H. Allen, 'Modeling the transition of microcracks into macrocracks in heterogeneous viscoelastic media using a two-way coupled multiscale model', *International Journal of Solids and Structures*, vol. 48, no. 22, pp. 3160–3175, Nov. 2011, doi: 10.1016/j.ijsolstr.2011.07.010.
- [23] V. Goyal and R. Jorge, 'Micro-Scale Crack Propagation Using the eXtended Finite Element Method', in *57th AIAA/ASCE/AHS/ASC Structures, Structural Dynamics, and Materials Conference*, 0 vols, American Institute of Aeronautics and Astronautics, 2016. doi: 10.2514/6.2016-0729.
- [24] M. Sharafisafa and M. Nazem, 'Application of the distinct element method and the extended finite element method in modelling cracks and coalescence in brittle materials', *Computational Materials Science*, vol. 91, pp. 102–121, Aug. 2014, doi: 10.1016/j.commatsci.2014.04.006.
- [25] L. Hedjazi, C. L. Martin, S. Guessasma, G. Della Valle, and R. Dendievel, 'Application of the Discrete Element Method to crack propagation and crack branching in a vitreous

- dense biopolymer material’, *International Journal of Solids and Structures*, vol. 49, no. 13, pp. 1893–1899, Jun. 2012, doi: 10.1016/j.ijsolstr.2012.03.030.
- [26] L. Scholtès and F.-V. Donzé, ‘A DEM model for soft and hard rocks: Role of grain interlocking on strength’, *Journal of the Mechanics and Physics of Solids*, vol. 61, no. 2, pp. 352–369, Feb. 2013, doi: 10.1016/j.jmps.2012.10.005.
- [27] F. Kun, G. Pál, I. Varga, and I. G. Main, ‘Effect of disorder on the spatial structure of damage in slowly compressed porous rocks’, *Philosophical Transactions of the Royal Society A: Mathematical, Physical and Engineering Sciences*, vol. 377, no. 2136, p. 20170393, Jan. 2019, doi: 10.1098/rsta.2017.0393.
- [28] P. A. Cundall, ‘Formulation of a three-dimensional distinct element model—Part I. A scheme to detect and represent contacts in a system composed of many polyhedral blocks’, *International Journal of Rock Mechanics and Mining Sciences & Geomechanics Abstracts*, vol. 25, no. 3, pp. 107–116, Jun. 1988, doi: 10.1016/0148-9062(88)92293-0.
- [29] Itasca Consulting Group Inc., ‘PFC2D/3D Version 6.0 Documentation’. Itasca Consulting Group Inc., 2020.
- [30] P. A. Cundall and O. D. L. Strack, ‘A discrete numerical model for granular assemblies’, *Géotechnique*, vol. 29, no. 1, pp. 47–65, Mar. 1979, doi: 10.1680/geot.1979.29.1.47.
- [31] J. Rojek, E. Oñate, C. Labra, and H. Kargl, ‘Discrete element simulation of rock cutting’, *International Journal of Rock Mechanics and Mining Sciences*, vol. 48, no. 6, pp. 996–1010, Sep. 2011, doi: 10.1016/j.ijrmms.2011.06.003.
- [32] N. Cho, C. D. Martin, and D. C. Segol, ‘A clumped particle model for rock’, *International Journal of Rock Mechanics and Mining Sciences*, vol. 44, no. 7, pp. 997–1010, Oct. 2007, doi: 10.1016/j.ijrmms.2007.02.002.
- [33] D. Potyondy, ‘A flat-jointed bonded-particle material for hard rock’, presented at the 46th U.S. Rock Mechanics/Geomechanics Symposium, Jan. 2012. Accessed: Jul. 09, 2020. [Online]. Available: <https://www.onepetro.org/conference-paper/ARMA-2012-501>
- [34] D. Potyondy, ‘A Flat-Jointed Bonded-Particle Model for Rock’, presented at the 52nd U.S. Rock Mechanics/Geomechanics Symposium, Aug. 2018. Accessed: Apr. 28, 2020. [Online]. Available: <https://www.onepetro.org/conference-paper/ARMA-2018-1208>
- [35] G. Papanicolau, A. Bensoussan, and J.-L. Lions, *Asymptotic Analysis for Periodic Structures*. Elsevier, 1978.
- [36] L. Brochard, T. Honório, M. Vandamme, M. Bornert, and M. Peigney, ‘Nanoscale origin of the thermo-mechanical behavior of clays’, *Acta Geotech.*, vol. 12, no. 6, pp. 1261–1279, Dec. 2017, doi: 10.1007/s11440-017-0596-3.
- [37] M. P. Allen and D. J. Tildesley, *Computer Simulation of Liquids*. Oxford University Press, 1987.
- [38] P. A. Cundall, ‘Computer Simulations of Dense Sphere Assemblies’, in *Studies in Applied Mechanics*, vol. 20, M. Satake and J. T. Jenkins, Eds. Elsevier, 1988, pp. 113–123. doi: 10.1016/B978-0-444-70523-5.50021-7.
- [39] I. Agnolin and J.-N. Roux, ‘Internal states of model isotropic granular packings. I. Assembling process, geometry, and contact networks’, *Phys. Rev. E*, vol. 76, no. 6, p. 061302, Dec. 2007, doi: 10.1103/PhysRevE.76.061302.
- [40] S. Emam, ‘Technical memorandum: Distortion of the Periodic Space in PFC, PFC Documentation Set’. Itasca Consulting Group Inc., 2009.
- [41] J. Christoffersen, M. M. Mehrabadi, and S. Nemat-Nasser, ‘A micromechanical description of granular material behavior’, *J. Appl. Mech.*, vol. 48, no. 2, pp. 339–344, Jun. 1981, doi: 10.1115/1.3157619.

- [42] Vallejos Javier Andres, Salinas José Matias, Delonca Adeline, and Mas Ivars Diego, ‘Calibration and Verification of Two Bonded-Particle Models for Simulation of Intact Rock Behavior’, *International Journal of Geomechanics*, vol. 17, no. 4, p. 06016030, Apr. 2017, doi: 10.1061/(ASCE)GM.1943-5622.0000773.
- [43] C. Zhou, C. Xu, M. Karakus, and J. Shen, ‘A systematic approach to the calibration of micro-parameters for the flat-jointed bonded particle model’, *Geomechanics and Engineering*, vol. 16, no. 5, pp. 471–482, 2018, doi: 10.12989/gae.2018.16.5.471.
- [44] D. Potyondy, ‘Technical memorandum: Material-Modeling Support for PFC, PFC 6 Documentation Set’. Itasca Consulting Group Inc., 2019.
- [45] R. F. S. Hearmon, ‘An introduction to applied anisotropic elasticity’, *The Mathematical Gazette*, vol. 48, no. 363, pp. 129–129, Feb. 1964, doi: 10.2307/3614376.
- [46] A. F. Bower, *Applied Mechanics of Solids*. CRC Press, 2009.
- [47] S. Brisard, L. Dormieux, and D. Kondo, ‘Hashin–Shtrikman bounds on the bulk modulus of a nanocomposite with spherical inclusions and interface effects’, *Computational Materials Science*, vol. 48, no. 3, pp. 589–596, May 2010, doi: 10.1016/j.commatsci.2010.02.027.
- [48] C. Tucker and E. Liang, ‘Stiffness Predictions for Unidirectional Short-Fiber Composites: Review and Evaluation’, *Composites Science and Technology*, pp. 59–655, 1999.
- [49] R. S. Lakes, *Viscoelastic Solids*. CRC Press, 1998. doi: 10.1201/9781315121369.
- [50] W. Pabst and E. Gregorová, ‘Effective elastic properties of alumina-zirconia composite ceramics - part 2. Micromechanical modeling’, p. 10, 2004.
- [51] Y. Joliff, J. Absi, M. Huger, and J. C. Glandus, ‘Experimental and numerical study of the room temperature elastic modulus of model materials with partly bonded matrix/particles interfaces’, *Computational Materials Science*, vol. 39, no. 2, pp. 267–273, Apr. 2007, doi: 10.1016/j.commatsci.2006.06.005.
- [52] Z. Živcová, M. Černý, W. Pabst, and E. Gregorová, ‘Elastic properties of porous oxide ceramics prepared using starch as a pore-forming agent’, *Journal of the European Ceramic Society*, vol. 29, no. 13, pp. 2765–2771, Oct. 2009, doi: 10.1016/j.jeurceramsoc.2009.03.033.
- [53] D. André, B. Levraut, N. Tessier-Doyen, and M. Huger, ‘A discrete element thermo-mechanical modelling of diffuse damage induced by thermal expansion mismatch of two-phase materials’, *Computer Methods in Applied Mechanics and Engineering*, vol. 318, pp. 898–916, May 2017, doi: 10.1016/j.cma.2017.01.029.
- [54] W. Pabst, T. Uhlířová, E. Gregorová, and A. Wiegmann, ‘Young’s modulus and thermal conductivity of model materials with convex or concave pores – from analytical predictions to numerical results’, *Journal of the European Ceramic Society*, vol. 38, no. 7, pp. 2694–2707, Jul. 2018, doi: 10.1016/j.jeurceramsoc.2018.01.040.